5-2008

On New Applications and Sensitivity Enhancement of Cantilever-based Sensing Systems

Calvin Bradley
Clemson University, calvinb@clemson.edu

ON NEW APPLICATIONS AND SENSITIVITY ENHANCEMENT OF CANTILEVER-BASED SENSING SYSTEMS

A Thesis
Presented to
the Graduate School of
Clemson University

In Partial Fulfillment
of the Requirements for the Degree
Master of Science
Mechanical Engineering

By
Calvin Rhett Bradley
May 2008

Accepted by:
Dr. Nader Jalili, Committee Chair
Dr. Darren M. Dawson
Dr. Mohammed F. Daqaq

ABSTRACT

Cantilever-based Sensing Systems (CSS) have become a focal area for research with the rise of micro- and nanotechnology. History has led us to use cantilever beams as one of the foremost sensing devices for small scale applications, beginning with the atomic force microscopy, and then being expanded into numerous sensor devices. The CSS include such applications as accelerometers, thermal and chemical sensors which are expanding into the applications of mass sensing and material characterization. Soon, this technology may be used in “lab on chip” biosensing applications.

This study covers the experimentation into new CSS applications and sensitivity enhancement. In order to do this, an overview of CSS is presented. The history of cantilever is covered from its humble beginnings to the recent explosion of interest. Next, working principles, operational modes and microfabrication of the CSS are briefly overviewed. Experimentation into novel CSS applications for material characterization of a thermally sensitive polymer is discussed first. To accomplish this, an array of cantilevers is used to isolate effect of the polymer. The results show that static mode CSS using optical transduction can be effectively used to sense polymers lower critical solution temperature via measuring the beam deflection caused by surface stress due to the polymer instead of repeated traditional surface hydrophobicity tests.

In the next part of the thesis, a new CSS design is fabricated and used for mass detection. This new design utilizes stress measurements of an integrated strain gauge with reference cantilever. The new design allows for the measurement of the frequency shift while compensating for environmental effects. The CSS design is characterized and tested utilizing the addition of Au nanoparticles as functional added mass.

The final section of this study focuses on an exciting new CSS sensitivity enhancement technique. This new technique utilizes a delayed feedback to create stable limit cycles. The amplitude of these limit cycles is shown to be highly sensitive to changes in tip mass added or attached to the cantilever. The theory is presented and verified utilizing macroscale experimentation. Both theoretical and experimental results demonstrate a two-orders-of magnitude sensitivity enhancement over traditional frequency shift methods.

DEDICATION

For my father who has been my greatest role model, advisor, guide and friend.

ACKNOWLEDGEMENTS

I have been extremely blessed by having Dr. Nader Jalili as my advisor. He has been patient and motivating, and always exceeded my expectations of a professor. I was very fortunate to work extensively with Dr. Mohamed F. Daqaq, whose mastery of his field is rivaled only by his willingness to teach his art to others. I would also like to thank Dr. Dawson for serving on my advisory committee. In addition to these men I must thank Dr. Ruediger Berger of Max-Planck Institute for Polymer Research and Dr. Zachary Davis of the Technical University of Denmark who I was fortunate enough to work with. Along the way I have become indebted to many friends from Max-Planck Institute for Polymer Research, Technical University of Denmark, and everyone from Clemson's SSNEMS laboratory for their invaluable help. I thank the National Science Foundation's IREE program for supporting me financially during my research abroad and Dr. Wagner for serving as my supervisor during my teaching experience.

TABLE OF CONTENTS

LIST OF FIGURES

FIGURE PAGE

CHAPTER 1 : MOTIVATION AND PROBLEM STATEMENT

Motivation

The world continues to change at a rapid pace. People expect everything faster, smaller, and more reliable. Why shouldn't we? Not long ago everyone had to dial a phone number on a bulky phone to connect to another bulky phone at a fixed location. Now we call, send messages, photos or video to a small personal phone that is carried with us at all times. All this we have come to expected without compromising performance or reliability.

This same trend occurs for sensing systems. Currently, it takes a room of equipment and a number of technician's several hours to test for bacteria, viruses, or to run other biological tests. In the future, however, we want to be able to do more than we are currently able. We want to be able to do it faster and we want to be able to put it in a box that can be taken to remote locations. This is the same thing that has happened with phones. In order to accomplish this goal, sensor systems must evolve. The transition from the original telephone to the mobile phones today was not a single improvement to phone technology but a continual process of rethinking and improving on existing functional system. The same must be done with sensor systems.

To advance the state of the art for sensing system's the desire is to give them more applications and to make them cheaper, smaller, and more sensitive. This makes the micro- and nano-scale fabrication and characterization techniques more attractive because making a smaller sensor can not only decrease size and cost but it can be more sensitive as well. Cantilever-based Sensing Systems (CSS) are an area that has become a hotbed of interest because they can address these issues. Because of this, the number of applications for CSS is increasing and the amount of research for better and smaller CSS is growing in order to fulfill future demands and requirements.

Problem Statement and Objectives

A CSS is a trivial sensor on the macroscale but as the scale decreases, the usefulness increases. Micro CSS have found usefulness in various applications. However, CSS are not unique for all types of systems; each application has different requirements. A transduction method that is ideal for one application may fall short for another; and what is sufficient sensitivity for one application will be insufficient for another. In order to determine what type of sensor is ideal for a given application, an understanding of the principles for various configurations and modes of CSS must be understood.

The objective of this thesis is to provide an overview on CSS, to illustrate usefulness of CSS in novel applications, and to demonstrate a new delayed feedback operating mode that provides a tunable, yet ultrasensitive CSS.

Thesis Overview and Contributions

An overview of CSS is given in Chapter 2. We will begin with the history from CSS roots then continue to the state of the art. The working principles of CSS are then covered to provide the necessary background. This is followed by an introduction of the two basic modes of operation. Following this, the transduction methods and fabrication techniques for CSS are introduced.

Chapter 3 deals with a new application for the first operational mode of CSS. In order to understand this new application, an introduction into PNIPAM thermally sensitive polymers is given. The experimental setup illustrates the usefulness of a multi-cantilever array using reference beams to isolate functional effects. Results demonstrate the usefulness of CSS in this new application. The test also shows some of the difficulties with current techniques.

Chapter 4 covers the fabrication and testing of new cantilever design with a transduction method utilizing an integrated strain gauge. This advancement resolves some of the issues with optical transduction methods by decreasing the size and cost of apparatus while still correcting for environmental effects. These new cantilevers are tested using the second operational mode for CSS to detect the presents of Au nanoparticles.

Chapter 5 deals with advancing the primary function of CSS, the sensitivity. This is accomplished utilizing a time-delayed feedback strategy. Effects of time-delay are discussed by looking at first the linear, then nonlinear problem. This results in a possibility for a limit cycle that has amplitude much more sensitive to additional mass than traditional methods of utilizing frequency changes. The problem is solved utilizing the method of multiple scales. Then, the method for tuning the sensitivity is discussed.

The delayed feedback method is demonstrated utilizing two different macro CSS and stability results are compared with theoretical findings. Results for the new method are compared with the traditional method. Finally, Chapter 6 gives a summary of the thesis and conclusions, followed by future work section.

CHAPTER 2 : OVERVIEW OF CANTILEVER-BASED SENSING SYSTEM (CSS)

Overview of CSS

The cantilever is common, naturally occurring, and fundamental structure. Typically, these structures are not used as sensors on the macroscale; however, on the micro and smaller scales, they surpass other methods for many sensing applications. The relatively short history of micro CSS began with the desire to explore surfaces with molecular resolution and has rapidly grown to applications ranging from accelerometers to chemical and biosensors.

Cantilevers are frequently seen in our day to day lives. From tree limbs to flag poles and diving boards to buildings they are everywhere. The cantilever is defined as beam with one end fixed and the other free (as illustrated in Figure 2.1). While on the macroscale they would be trivial for use as sensors. However, as scale decreases, the relevance of these structures as sensors increases. On the macroscale other methods for sensing are superior. An example would be sophisticated mass balances utilizing precise standards can be utilized [1] for mass sensing. However, these principles become impossible to implement as scale is reduced. However, the operating principles for the cantilever are simple enough that they can be scaled down to detect masses on a much smaller scale. While other small scale mass detection, such as quartz crystal microbalance (QCM) techniques, achieve sensitivity on the nanogram and picogram range [2], micro CSS are entering into the zeptogram scale sensitivity [3, 4].

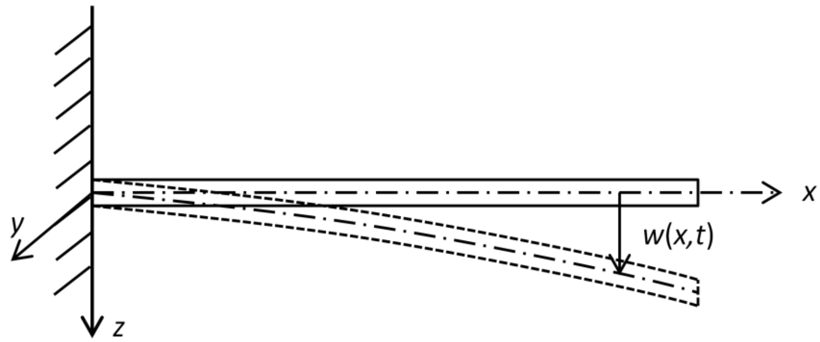

Figure 2.1 Basic cantilever showing a fixed left end and free right end. Transverse deflection is *w* from neutral axis.

The first use of a cantilever as a sensor was made by Galileo. He utilized cantilevers to determine the strength of the materials from which the cantilever was made [5]. However, the principles that most of today's sophisticated applications of CSS employ were not introduced until 1909 when Stoney introduced his equations relating surface stress to cantilever deflections [6]. Stoney used his cantilever for determining the surface stress caused by an electrochemical environment. Later, use of a cantilever sensor for gas detection was introduced by Taylor in the 1970's [7].

The technology of making cantilevers for microscale application was spurred by the introduction of scanning probe microscopy (SPM) and, in particular, atomic force microscopy (AFM). The AFM enables molecular resolution of surfaces. It uses a microcantilever with a sharp tip that probes the surface [8]. The transduction method for the behavior of this cantilever is typically a laser on the side opposite of the probe. In order to keep interaction forces small, it is ideal to have a cantilever with minimal stiffness. This forced the fabrication of small cantilevers with very low stiffness.

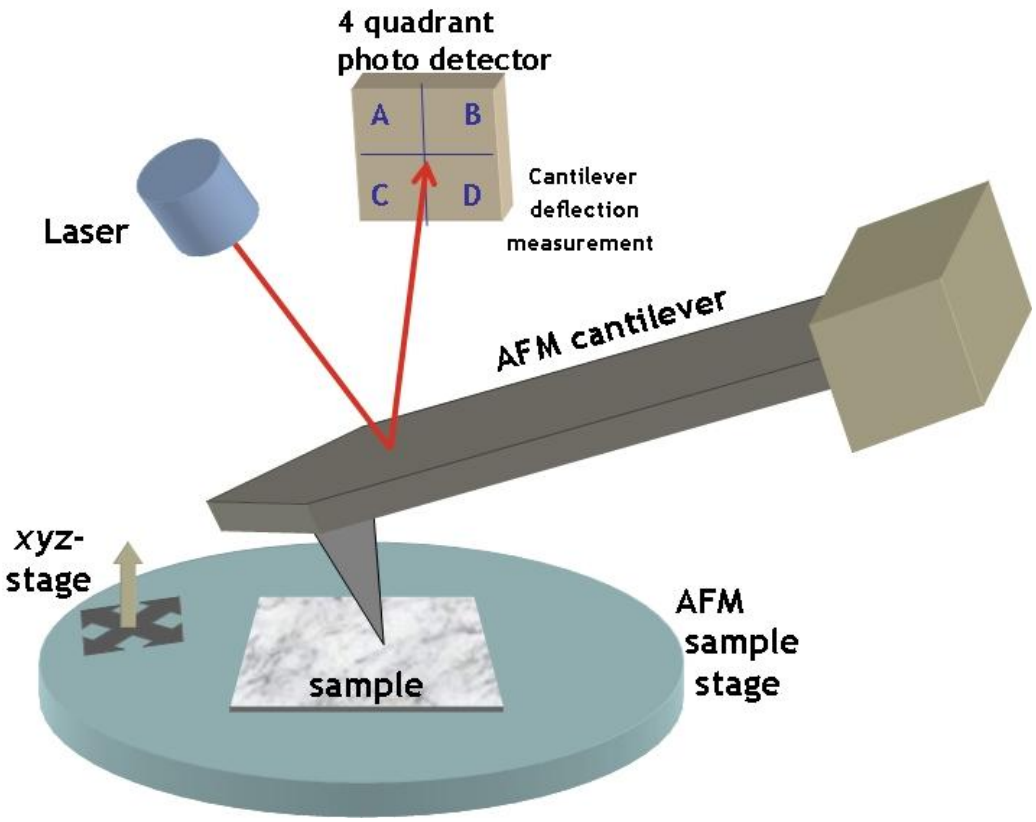

Figure 2.2 Working principles of a AFM showing laser transduction method and a sharp tip interacting with surface and multiple region photo sensitive detector [9].

A problem encountered by operators of AFM led to new applications for microcantilevers. It was noticed that vapor adsorption during operation led to problematic cantilever deflection [10]. Noticing this, Thundat et al. realized the possible use of micro CSS to detect added mass from water and mercury vapor [10].

At the same time Gimzewski, et al. began creating micro CSS to use as thermal sensors to monitor thermal reactions of chemicals [11]. Utilizing these devices, he was able to create a calorimeter with femtojoule sensitivity [12, 13].

These advances caused a great stir in the research field as many potential applications for microcantilevers in sensing systems emerged. Early CSS focused mainly on chemical [14, 15, 16, 17, 18] and thermal [19, 20, 21, 14, 22, 23] sensors. However, as interest in biotechnology increased, so did the uses for CSS. These applications are detection of small objects such as bacterial cells, proteins, and antibodies [24, 25, 26] as well as being used as a mechanism for DNA hybridization [27]. CSS have also impacted healthcare by providing a mechanism to measure blood glucose levels for diabetes diagnoses [28], identifying important cardiac muscle proteins indicative of myocardial infarction[29], and detecting antigens specifically used to monitor prostate cancer [30]. With the proven potential for label-free detection of complex biomolecular organisms and molecules, chemical applications for NMCS have rapidly evolved. Using these sensors, dangerous chemical agents such as toxic vapors [31] and chemical nerve weapons [32] have been precisely and accurately identified.

Working Principles of Micro CSS

The working principles of micro CSS can be divided into two areas, the dynamic mode(typically utilized for mass detection) and static mode (typically for surface stress measurement).

Koch and Abermann used what was termed a “beam bending” technique on thin plates around a millimeter to observe the changes in surface stress caused by the deposition of metallic films [33]. While not on the microscale, they illustrated the effectiveness of the mode for finding surface stress by the bending of a cantilevered structure.

Stoney introduced his simplification to determining thin film properties on a surface. The equation for surface stress σ_{St} is commonly expressed as

$$\sigma_{St} = \frac{E t_s^2}{6 t_c} K \tag{2-1}$$

where K is the curvature of the beam E is the modulus of the substrate and t_s, t_c are the thicknesses of substrate and coating respectively. The curvature of the beam is estimated from the tip deflection. The estimate for curvature can be given by:

$$K = \frac{d^2 w}{dx^2} \tag{2-2}$$

Approximating this for the case of the beam we find that

$$K = \frac{w}{L^2} \tag{2-3}$$

where w is the tip displacement of the beam ($w(L,t) = w$) and L is the length of the beam. This makes Stoney's equation as a function of displacement given by:

$$\sigma_{st} = \frac{E t_s^2 w}{6 t_c L^2} \tag{2-4}$$

This becomes a useful equation for the analysis of micro CSS. There are several methods for correcting the thin film model for a thicker film [34].

For a cantilever of given length, *L*, width, *b*, and height, *h*, such that the beam is slender meaning that the length is much larger than cross-section dimensions, the equation of motion can be described by Euler-Bernoulli beam by considering only axial strain and a uniform beam

$$\rho \mathrm{A} \frac{\partial^2 w(x,t)}{\partial t^2} + EI \frac{\partial^4 w(x,t)}{\partial x^4} = 0 \qquad \textbf{(2-5)}$$

where w describes the transverse displacement of the beam at the location along the length *x*, ρ is density, A is the cross-sectional area (*b***h*), *E* is Young's Modulus and I is the area moment of inertia [35]. Using the assumed solution

$$w(x,t) = W(x)e^{-i\omega_n t} \qquad \textbf{(2-6)}$$

and inserting into the equation of motion (2-5) yields the following ordinary differential equation (ODE) for spatial function W(x):

$$\frac{d^4 W(x)}{dx^4} = \frac{\omega_n^2 \rho \mathrm{A}}{EI} W(x) \qquad \textbf{(2-7)}$$

By defining the boundary conditions for the cantilever beam

$$w(0,t) = 0 \qquad \textbf{(2-8)}$$

$$\left. \frac{\partial w(x,t)}{\partial x} \right|_{x=0} = 0 \qquad \textbf{(2-9)}$$

$$\left.\frac{\partial w^2(x,t)}{\partial x^2}\right|_{x=L} = 0 \qquad \textbf{(2-10)}$$

$$\left.\frac{\partial w^3(x,t)}{\partial x^3}\right|_{x=L} = 0 \qquad \textbf{(2-11)}$$

the solution to the spatial function *W(x)* results in, so-called, eigenfunctions [36]

$$W_n(x) = A_n(\cos K_n x - \cosh K_n x) + B_n(\sin K_n x - \sinh K_n x)$$

$$K_n = \left(\frac{\omega_n^2 \rho \mathrm{A}}{EI}\right)^{1/4} \qquad \textbf{(2-12)}$$

$$\frac{A_n}{B_n} = -1.362, -0.982, -1.001, -1, \dots$$

Where *n* is the modal number. Modal frequencies K_n are determined from:

$$\cos K_n L \cosh K_n L = -1$$
$$K_n L = 1.875, 4.694, 7.855, 10.996, \dots \qquad \textbf{(2-13)}$$

The eigenfunctions are normalized such that $A_n = 1$ this orthonormality conditions is states as

$$\int_0^L W_m(x) W_n(x) dx = \delta_{mn} \qquad \textbf{(2-14)}$$

where the δ_{mn} is the Kronecker delta. The first four eigenmodes can then be shown to take the form of Figure 2.3.

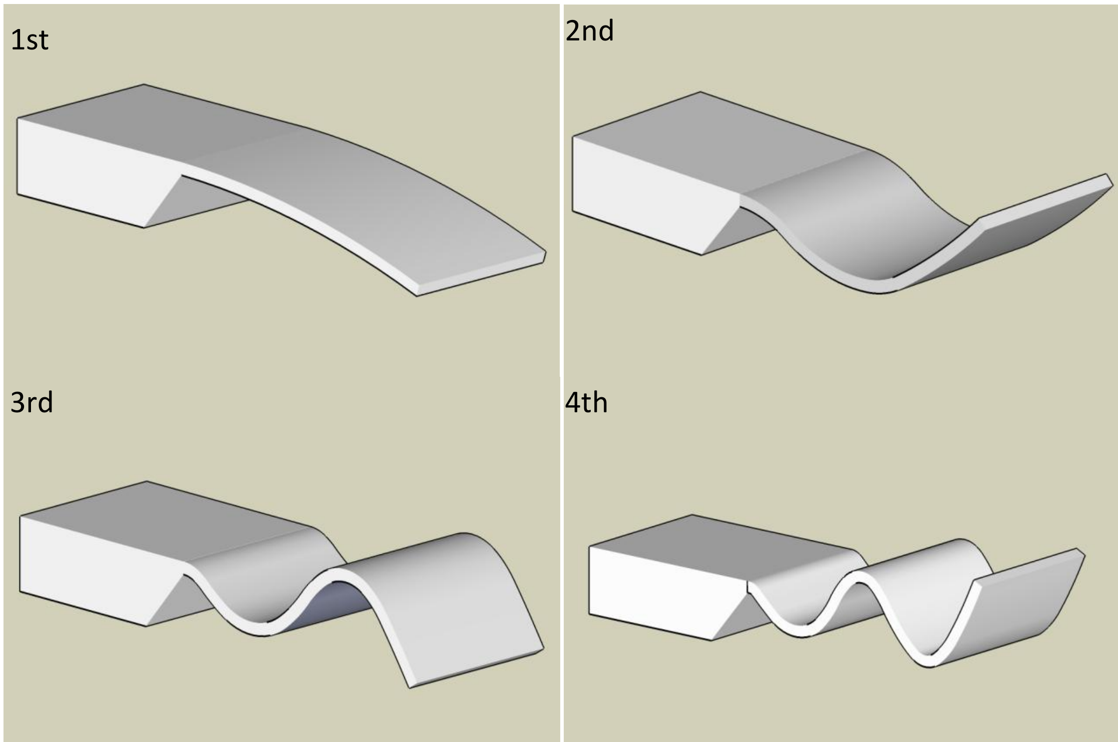

Figure 2.3 First four eigenmode shapes of cantilever.

For the standard case where a rectangular, uniform cantilever is being used we have [37]

$$I_{beam} = \int_{-b/2}^{b/2}\int_{h/2}^{h/2} z^2 dz dy = \frac{h^3 b}{12} \quad \textbf{(2-15)}$$

$$\omega_n = \frac{(K_n L)^2}{L^2}\sqrt{\frac{EI}{\rho \mathrm{A}}} = \frac{(K_n L)^2}{2\sqrt{3}}\frac{h}{L^2}\sqrt{\frac{E}{\rho}} \quad \textbf{(2-16)}$$

It is common to equate this to a harmonic resonator with an equivalent effective mass and stiffness terms.

$$m_{eff} = \frac{3m_0}{(K_n L)^4}, \qquad m_0 = \rho \mathrm{A} L, \qquad k = \frac{3EI}{L^3} \tag{2-17}$$

The resonant frequency of the beam is then simplified to

$$\omega_n = \sqrt{\frac{k}{m_{eff}}} \tag{2-18}$$

Operational modes of Micro CSS

A CSS has two operational modes. The static mode is conventionally used for sensing surface stresses, while the dynamic mode is utilized for the sensing of additional mass. Although these two effects are slightly coupled, it is small enough to normally be neglected.

For the static mode, the deflection of the cantilever is taken as the output of the system. Using Stoney's Equation (2-1) this is then related to the stresses acting upon the cantilever. This is useful in many sensing applications. Any reaction such as adsorption or absorption that can cause a layer to expand or seek to increase its surface area can be detected precisely [38, 39]. This is accomplished by the functionalization of one of the surfaces of the cantilever. This treatment causes the surface to show a high affinity to the target. The resulting changes in stress from the top to the bottom of the cantilever cause the deformation as seen in Figure 2.4 and Figure 2.5.

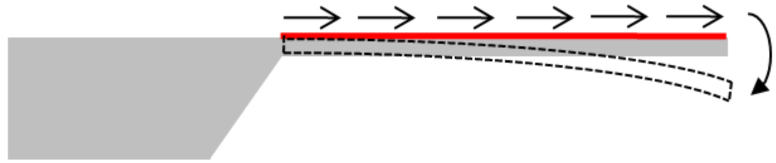

Figure 2.4 Stress in a functional layer causing deflection of the cantilever.

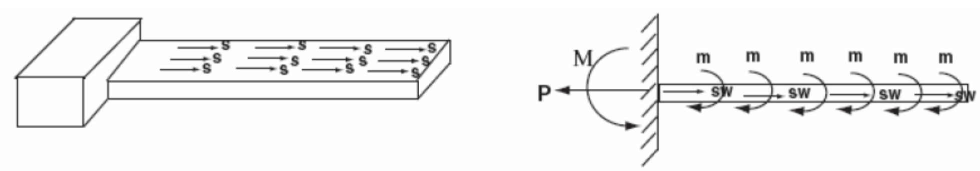

Figure 2.5 Modeling of surface stress on a cantilever [40]

A key advantage of Stoney's equation, along with a thin film assumption, is that the properties of the coating do not need to be known, just the coatings thickness. This makes it an ideal method for determining material properties.

The second mode is the dynamic or oscillating mode. This mode is typically used for the sensing of additional mass. As shown in Equation (2-18), the resonant or natural frequency of CSS is determined by the effective mass and the stiffness. When the mass of the CSS change's it leads to a resonant frequency shift. For this mode, the target can attach to either side of the cantilever and cause a change in the effective mass and thereby cause a shift in the resonant frequency. Because the sensitivity is based on the effective mass, and not just total mass, both the amount and location can affect the response characteristics and the frequency shift.

The resonant frequency of the beam is then simplified to

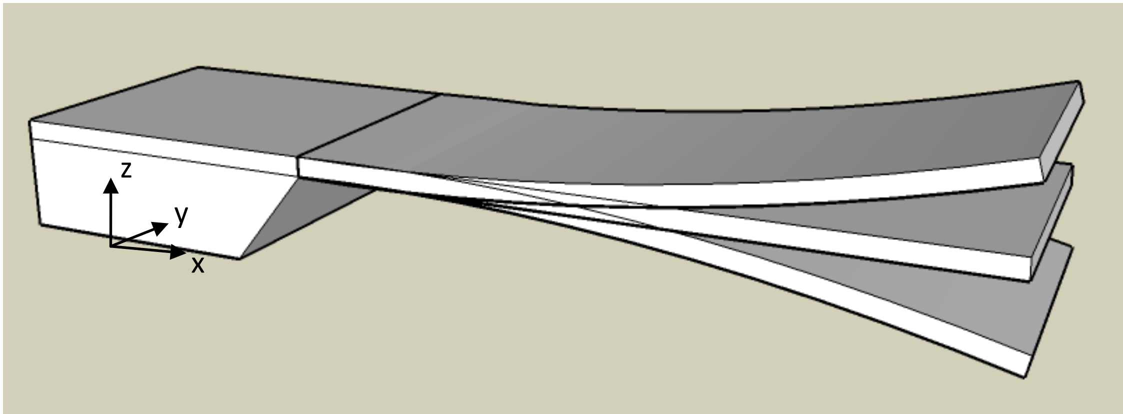

Figure 2.6 Resonating Cantilever in its first mode

Another critical issue that faces the use of dynamic mode for use as mass sensors is the ability to resolve resonance frequency. This is governed by the Q-factor which is a measurement of energy that is absorbed during oscillation. This is primarily governed by the damping of the dynamic mode. The Q-factor is defined as the total amount of energy stored in the oscillator divided by the energy lost during one cycle. We can write this as

$$Q = 2\pi \frac{E_{tot}}{\Delta E} \qquad \textbf{(2-19)}$$

where E_{tot} is the total dynamic energy of the of the system and ΔE is the amount of energy lost in one cycle.

The quality factor is often measured from the amplitude vs. frequency spectrum. In this method, the resonant frequency f_{res} is divided by the bandwidth, where the amplitude is at the 3dB (Δf_{3db}) as illustrated in Figure 2.7.

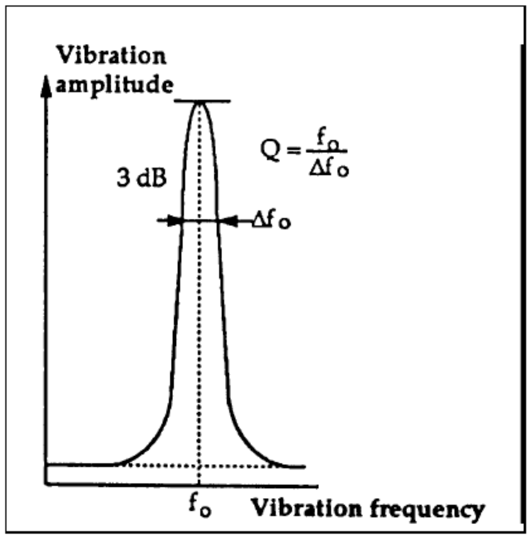

Figure 2.7 Q-factor calculation from the vibration amplitude vs. Frequency Spectrum [41]

If the quality factor for a dynamic CSS is low, the ability to resolve frequency shifts is also low as shown in Figure 2.8.

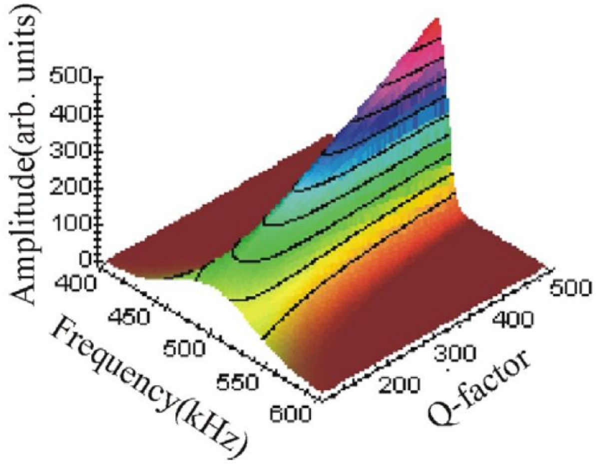

Figure 2.8 Q-factor determines the sharpness of the resonant frequency peak. [42]

In order to avoid these problems, many systems operate in a vacuum. This, however, eliminates many of the applications. Examples of these would be sensors for airborne elements or even more critical biosensor where the standard medium is water. In these cases, the energy dissipation causes signals to be difficult to obtain. Most critically is the lost ability to measure resonant frequency shifts. This becomes the limiting factor for sensitivity in dynamic mode mass sensing CSS. This problem can be addressed by utilizing the delayed feedback sensitivity enhancement presented in Chapter 5

Transduction Methods

The transduction of these two modes is accomplished by several methods. These include several forms of optical and electrical transduction techniques. Optical methods typically involve the use of an externally mounted laser that is reflected off the cantilever tip. This increases the size of the apparatus and tediousness of the CSS. This is due to bulky external lasers, lenses, mirrors and photo sensitive diode (PSD) that end up dwarfing the actual CSS. However, laser sensors can be configured in various ways lending to flexibility for applications. The electrical transduction techniques include capacitive and resistive based techniques. These can be integrated into the chip assembly reducing size and cost; however, these systems are more involved to design and lack some of the flexibility of the optical based system.

The optical transduction method is flexible as it has numerous methods by which it may be implemented. The most common setup is the laser reflecting off the cantilever tip and moving along a PSD as the cantilever deflects. An illustration of this is shown in Figure 2.9. This is a simple setup with one axis sensitivity. However, more sophisticated PSDs have multiple regions that can detect not only cantilever deflection but also when the cantilever is twisting as illustrated in Figure 2.2.

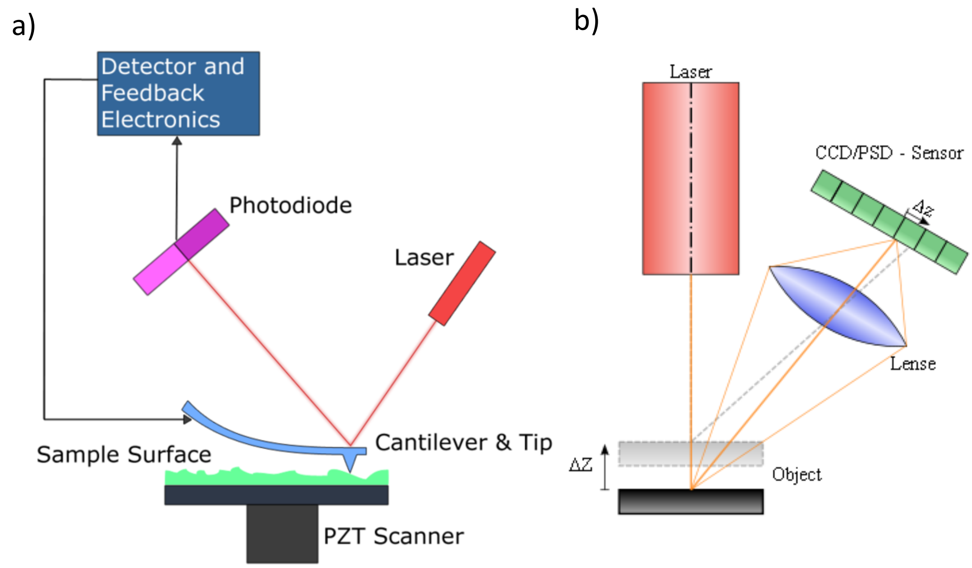

Figure 2.9 Example of a laser-based cantilever position transduction method from an a) AFM application [43] and a b) position sensor [44].

Another optical method that can be utilized is an interference approach. In this method, a laser is reflected off both a reference surface and the cantilever surface. When the cantilever returns, the interference causes the intensity to either increase or decrease as the two beams move in and out of phase with each other.

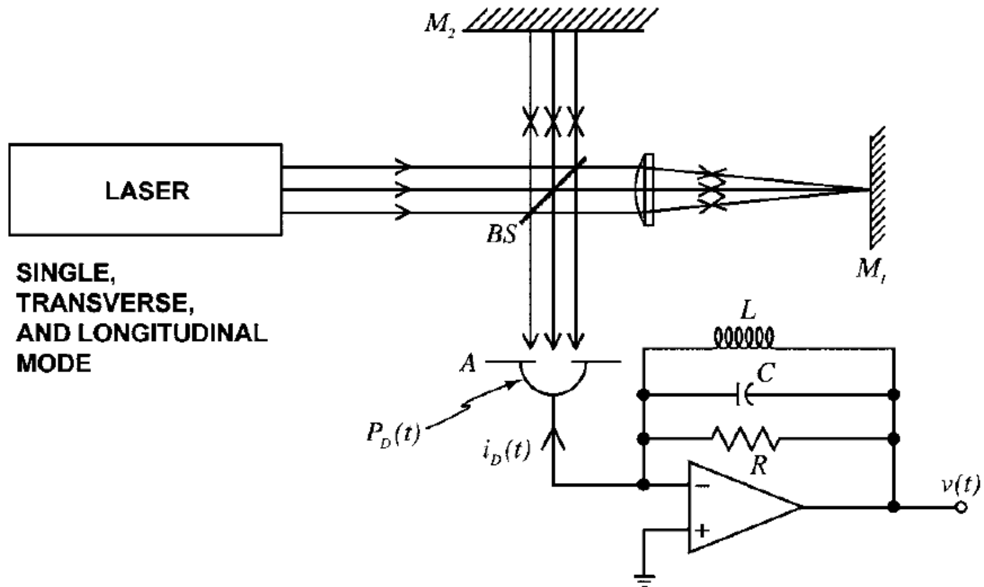

Figure 2.10 A simplified Michelson interferometer laser vibrometer [45].

Figure 2.10 depicts schematic of a Michelson interferometer laser vibrometer. The laser is reflected off the reference mirror labeled as M_2. This beam is added to the beam that is reflected by the signal mirror M_1 by the beamsplitter (BS). This produces an interfering beam with optical power $P_D(t)$ that is detected by the sensing apparatus with aperture A which produces the photocurrent $I_D(t)$ and the amplifier output voltage v(t) [45]. This method is ideal for static mode where deflection along the length of the cantilever is desired; however, it cannot take high sampling rates thereby it is limited for dynamic mode.

The other form of transduction involves electronic methods. These have the advantages of being smaller and less expensive than their laser-based counterparts. This is because the transduction components can be placed with the CSS and there is no laser to focus and keep pointed to the cantilever tip. With the benefit comes some additional complexity in the cantilever design. The principle that is examined in Chapter 4 is the resistance-based transduction method. The focal concept is that as a material undergoes a stress, the resistance changes. These changes are monitored and amplified utilizing modern circuit designs, and despite some level of complexity, can be placed in a small package and results can be gathered by standard lab equipment.

In addition to amplifiers and filters, a critical circuit element that is used to detect miniscule changes in resistance is the Wheatstone bridge. One of the primary advantages with this circuit is the necessity for very small currents in the sensors. This prevents heating and the destruction of components. Also, this can be utilized to compensate for such issues that arise from temperature shifts. This is accomplished by the use of a reference beam used in addition to the functional beam. The reference beam is exposed to all the same conditions as the functional beam with the exception of a lack of targeting agents. Thus, any shifts common to both beam, such as variation in temperature, are compensated and only changes due to functional elements are represented by the signal.

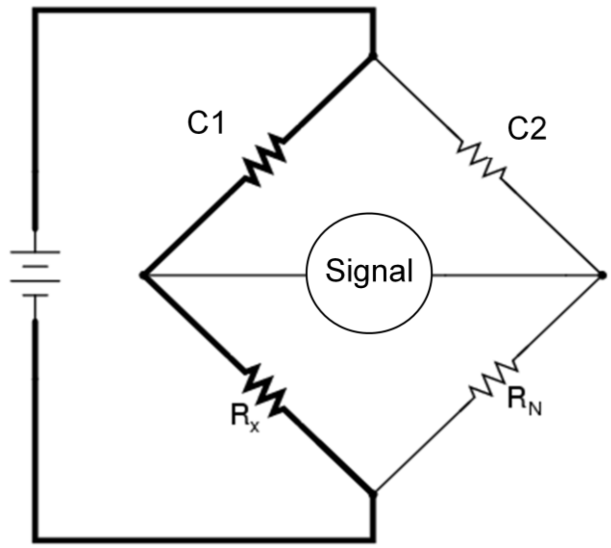

Figure 2.11 Illustration of a Wheatstone bridge circuit. With a properly balanced bridge a voltage will occur across the bridge when resistance ratios change caused by a change in the value of one of the resistors. C1 and C2 are functional and reference elements while R_x and R_n are tunable reference resistors.

Fabrication of Micro CSS

The usefulness of CSS are dependent on their size. The ability to manufacture CSS at a small scale makes them ideal for highly sensitive applications. Manufacturing at this small scale requires totally different techniques than those in macroscale applications. These include a combination of photolithography and thin film deposition and a combination of etching techniques. With these elements, cantilever structures can be manufactured in bulk with repeatable results on far smaller scales than those attainable with traditional machining techniques.

Photolithography is the technique of transferring patters by use of light. The word literally means printing with light. The technique can be simply understood as the casting of a shadow onto a surface with photo sensitive layer. The shadow is produced by a mask that is placed over the photosensitive layer.

This photosensitive layer in micro fabrication, called photoresist, changes its solubility with exposure. These photoresists fall into two categories. Positive photoresists include PMMA polymer (polymethlmethacrylate) and DQN copolymer Diazoquinone ester and phenolic novolak resin. When exposed to light, these layers become more soluble. This enables dissolved exposed layers but the remaining layer protects unexposed areas from etching processes. Negative photoresists include Bis (aryle)azide rubber and Kodak KFTR. These materials after exposure to light become more insoluble. Therefore, exposed areas are protected by remaining photoresist. The negative process is less effective for small geometry than the positive process. Hence, positive photolithography is the more common and preferred method. The two processes are illustrated in Figure 2.12.

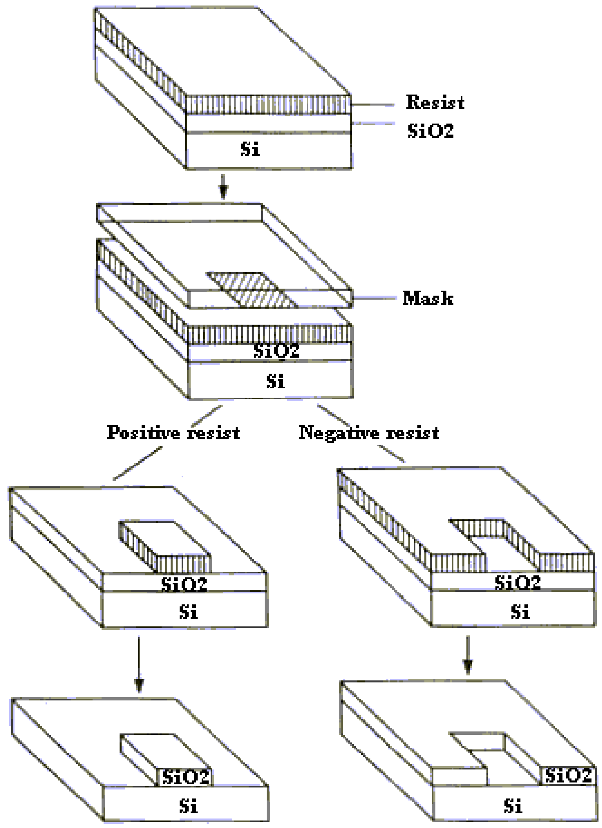

Figure 2.12 Examples of differences between positive and negative photolithography on a silicon substrate [46].

Fabrication typically begins with a substrate which forms the base of the device and, for nearly all micro devices, this substrate is composed of a silicon wafer. Thin films can be created on the substrate with two fundamental methods. The first is to grow a layer from the silicon itself. The other is a deposition of an additional material onto the substrate.

One of the simplest methods for producing a layer is to grow a layer of silicon oxide by the process of thermal oxidizing of surface of the silicon substrate. As oxygen reacts with the silicon, a layer of the desired silicon dioxide grows from the surface.

CHAPTER 3 : APPLICATION OF STATIC MODE CSS FOR DETECTING POLYMERS' LOWER CRITICAL SOLUTION TEMPERATURE

Introduction

Micro CSS have found applications in many diverse fields. Due to an extremely low stiffness' they have found use for determining the properties of materials at the microscale. One of these applications is material characterization. It is desired to explore the mechanical behavior of a polymer with novel properties. Utilizing a micro CSS in static mode, thermal effects on polymer properties were observed and a new method for determining the LCST of a PNIPAM polymer hydrogel layer is demonstrated. This chapter presents an overview of PNIPAM polymer and details the process of design and measurement.

PNIPAM background

Poly(N-isopropylacrylamide) (PNIPAM) is a fascinating and useful thermally sensitive polymer. The polymer is thermally sensitive due to its Lower Critical Solution Temperature (LCST). For this problem, the temperature at which this transition occurs is ideally between room temperature and body temperature. In this region, it is hoped that it can be utilized as a powerful drug delivery agent. Previous tests have demonstrated how polymer thickness and hydrophobicity change as the temperature is increased through this temperature [47]. These tests have shown the change in geometry (see Figure 3.1) and wettability or surface hydrophobicity (see Figure 3.2). Surface hydrophobicity is typically determined by contact angle tests [48].

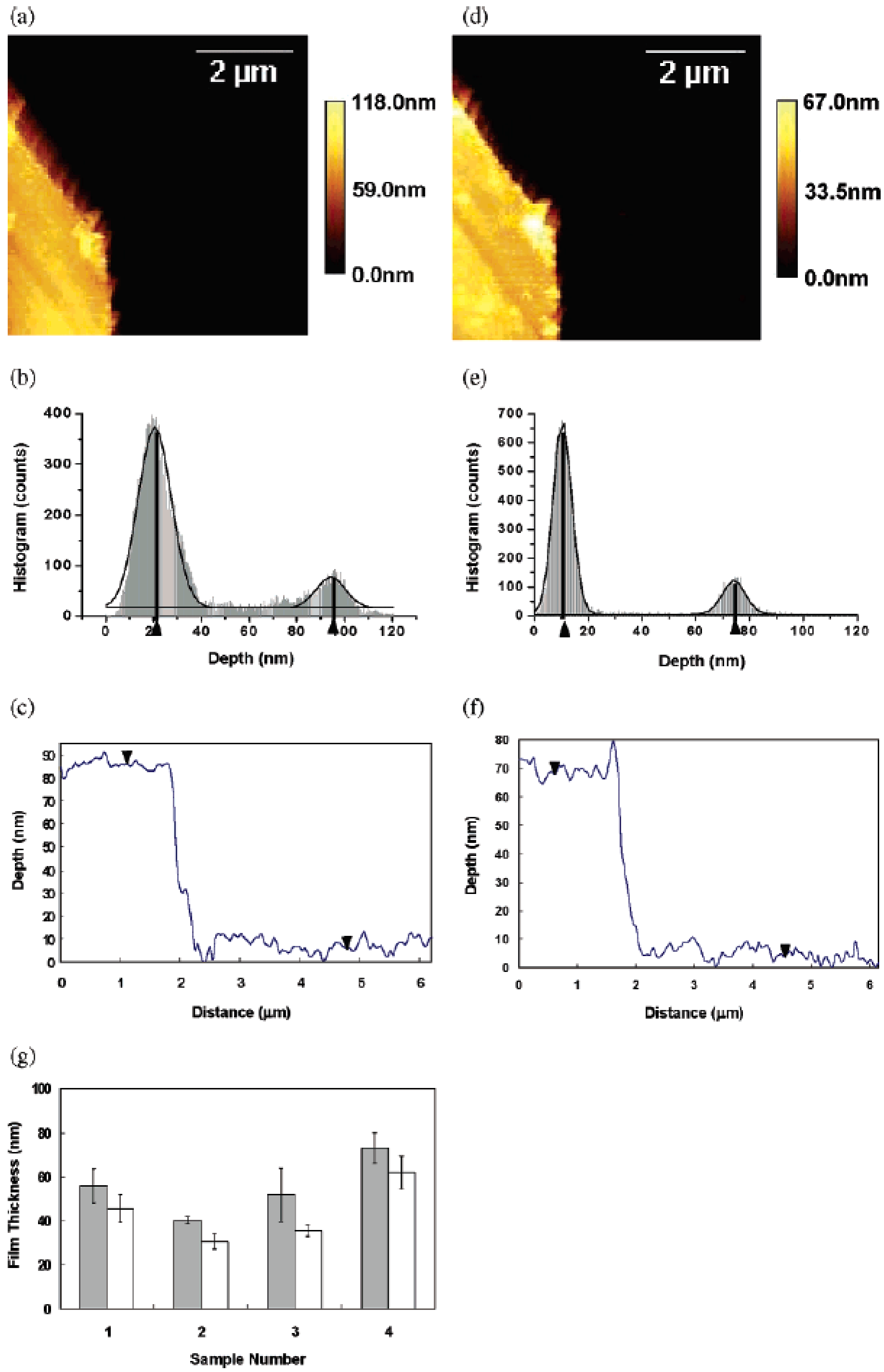

Figure 3.1 Results showing change in geometry of PMIPAM [49].

Results shown in Figure 3.1 are described by Cheng et al. as follows. "*AFM images of a ppNIPAM (PNIPAM) step on a silicon surface at 25 (a) and 37 °C (d). The corresponding height histograms (gray area) at 25 (b) and 37 °C (e) show two main heights, representing the substrate and plasma polymer surfaces, respectively. Each of the peaks is fitted to a Gaussian model (black curve), and the centers of the peaks are denoted by the triangular cursors. The step heights are obtained by subtracting the lower cursor position from the upper, giving a plasma polymer thickness of 73.7 nm at 25 °C and 63.7 nm at 37 °C for the scanned region. Section analyses on individual scan lines in each image are shown in (c) for 25 °C and (f) for 37 °C, which yields step heights of 74.2 and 63.1 nm, respectively. Film thickness measured on four different samples and three spots on each samples is summarized in (g) using the histogram analysis. The gray bar and white bar are film thicknesses measured at 25 and 37 °C, respectively, and a thicker film is observed for all measurements at 25 °C*" [49].

From these results it can be seen that as the polymer changes through the LCST, the thickness of the layer changes as well.

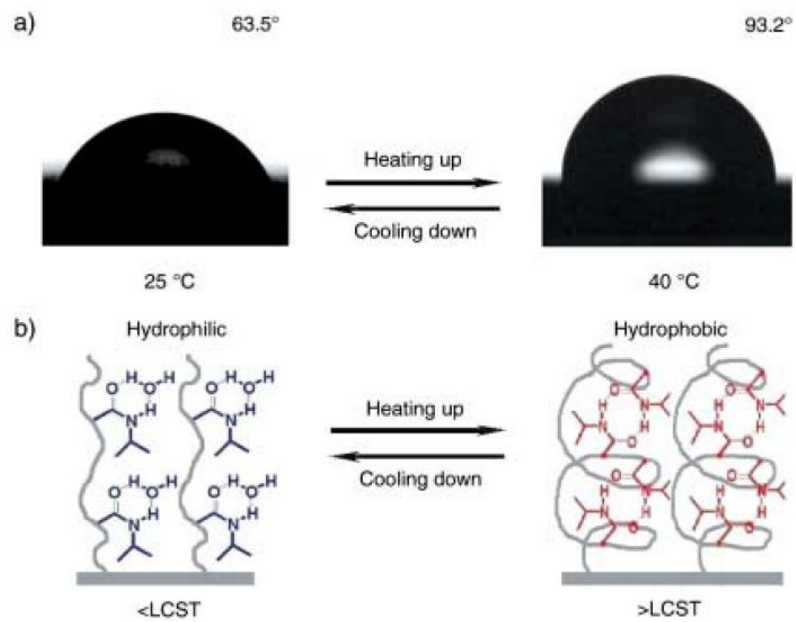

Figure 3.2 Wettability for a PNIPAM surface is shown. a) The Change of contact angles of a water droplet as temperature is changed from below to above the LCST. b) The intermolecular hydrogen bonding below LCST bonding between water and polymer chains is favorable, above LCST intermolecular bonding between C=0 and N-H collapses the chain [48].

The LCST occurs when it becomes thermodynamically favorable to break the hydrogen bonds with the water and create intermolecular hydrogen bonding between the C=0 and N-H groups. The change causes the chain to favor interaction with itself over the surrounding water inducing a dehydration of the polymer. This causes a coil to globule (a mushroom like shape) transition that collapses the chain as illustrated in Figure 3.2 and Figure 3.4.

Previous literature shows the transition of the surface properties change rapidly from hydrophobic to hydrophilic at the LCST as shown by contact angle tests. Contact Angle testing however only depends on the surface properties of the polymer. The full layer transition occurs more gradually. The dehydration and phase transition begins at temperatures lower than the LCST as shown by volume tests [50] as depicted in Figure 3.3.

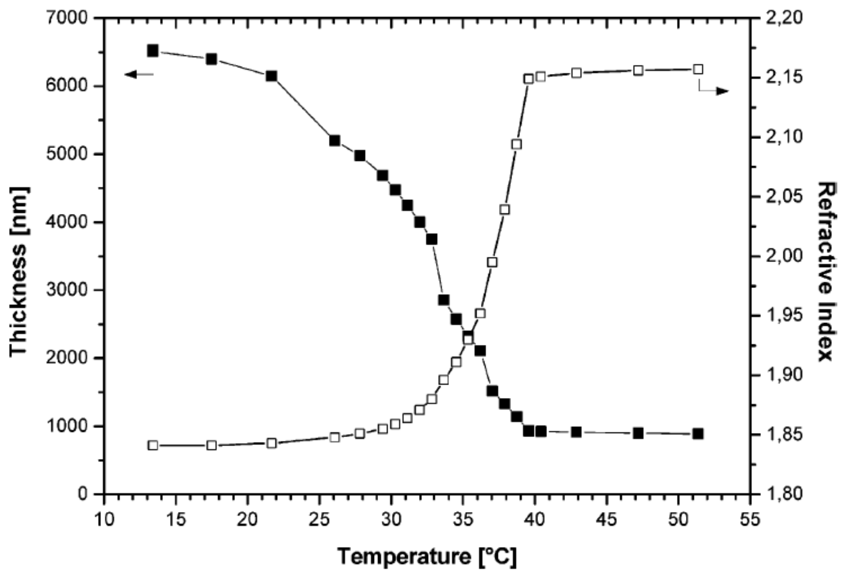

Figure 3.3 Temperature-dependant swelling behavior of a PNIPAM polymer across the LCST shows a range of temperature over which dehydration occurs [50].

How the mechanical properties behave as the transition through the LCST between hydrophilic and hydrophobic occurs is still largely unknown. This raises interest in detecting this transition utilizing mechanical methods. This is where a CSS becomes a novel new method for monitoring the mechanical nature of the transition of the phase states.

The configuration of polymers plays a significant part in their mechanical behavior. Figure 3.4 illustrates various configurations of polymers and their transition from the hydrophobic to hydrophilic state.

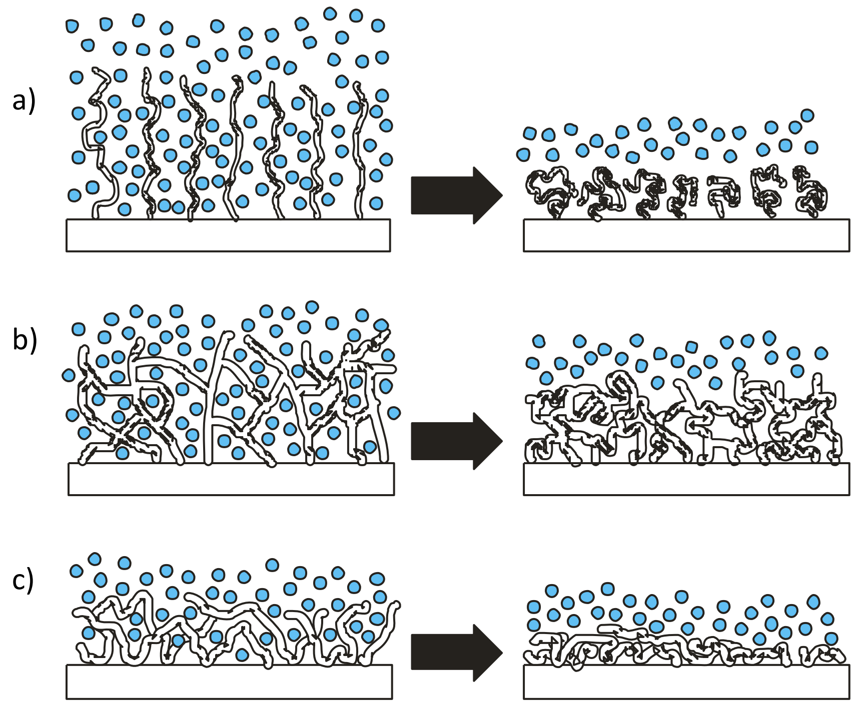

Figure 3.4 Polymer configurations before and after hydrophobicity transition. a) Grafted from surface polymer brush, b) plasma deposition polymer with cross linking and c) grafted too surface polymer no cross linking and lower grafting density.

In a hydrophilic state, the polymer brush configuration has relatively parallel chains extending into the fluid. In the hydrophobic state, these chains collapse onto themselves forming globules. If these brushes have a high enough grafting density, it is hypothesized that these globules interact with each other upon collapse.

The cross-linked plasma deposited polymer has a more random configuration with cross linking occurring as shown in Figure 3.4. These polymer chains and branches interlink to form a mesh that is swollen below the LCST with water being absorbed into the mesh. As temperature increases above the LCST, the mesh contracts as water is expelled. The layer is isotropic; however, due to grafting to bonding on the surface, collapse is constrained in the plane parallel to the substrate to which the polymer is attached.

The final configuration is a grafted to surface non-cross linked configuration. This method creates a much lower grafting density in addition to not having a cross linked mesh. This allows for a more freedom for the chains during transition.

Experimental Setup

Arrays of micro CSS were partially functionalized with the PNIPAM polymers. Three polymer configurations were tested utilizing micro CSS. These included the previously discussed polymer brush, plasma and grafting to configurations. A schematic of the fabrication of these configurations is demonstrated in Figure 3.5.

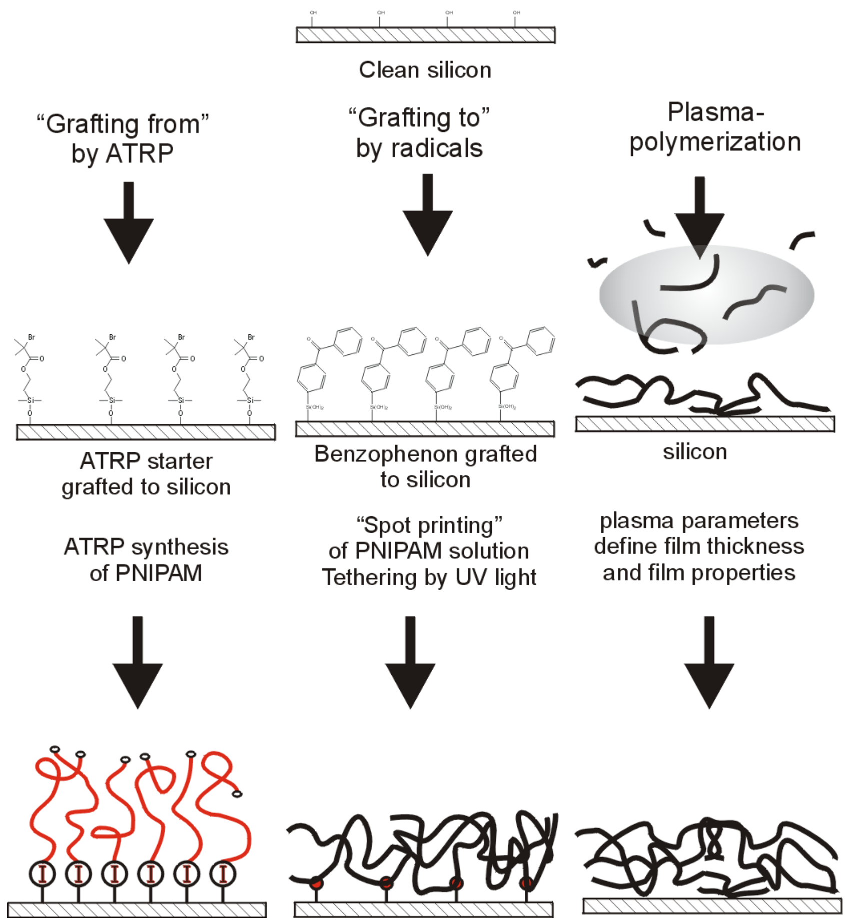

Figure 3.5 Depositions of polymers for polymer brush, plasma and grafting too configurations [51].

Non-functionalized cantilevers in array were protected from polymer deposition. A cantilever chip with 8 identical cantilevers was used. Four functional cantilevers are prepared with the polymer to be tested deposited on their upper surface and the remaining four cantilevers remain clean and used as references. During polymer deposition, reference cantilever surfaces were protected from polymer by either a chemical layer that was removed later or masked during deposition as shown in Figure 3.6.

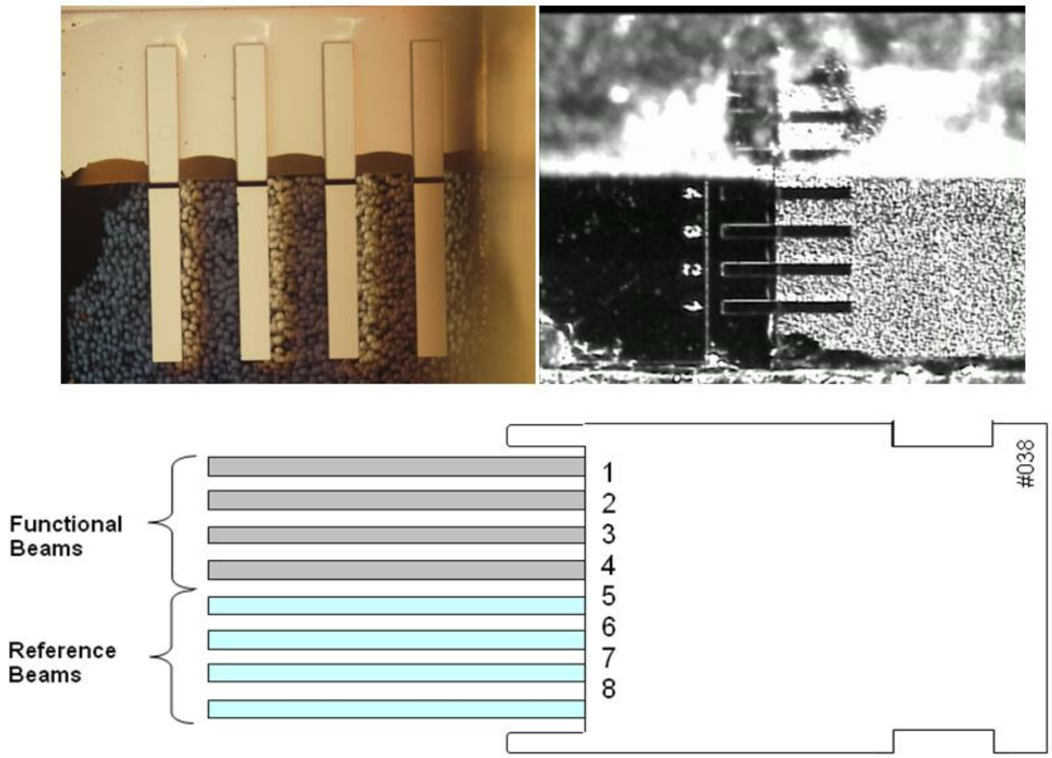

Figure 3.6 Cantilevers staged for plasma deposition using a masking method for protecting bottom surface and reference cantilever from polymer deposition. Upper images show a glass slide covering cantilevers 5 through 8 and a piece of silicon wafer under cantilevers protecting them from polymer deposition on the underside of the beam.

These are placed in a water filled chamber and deflection is monitored utilizing a Sentris cantilever monitoring system that operates utilizing a scanning laser and photo sensitive diode. The Sentris operation area is shown in Figure 3.7.

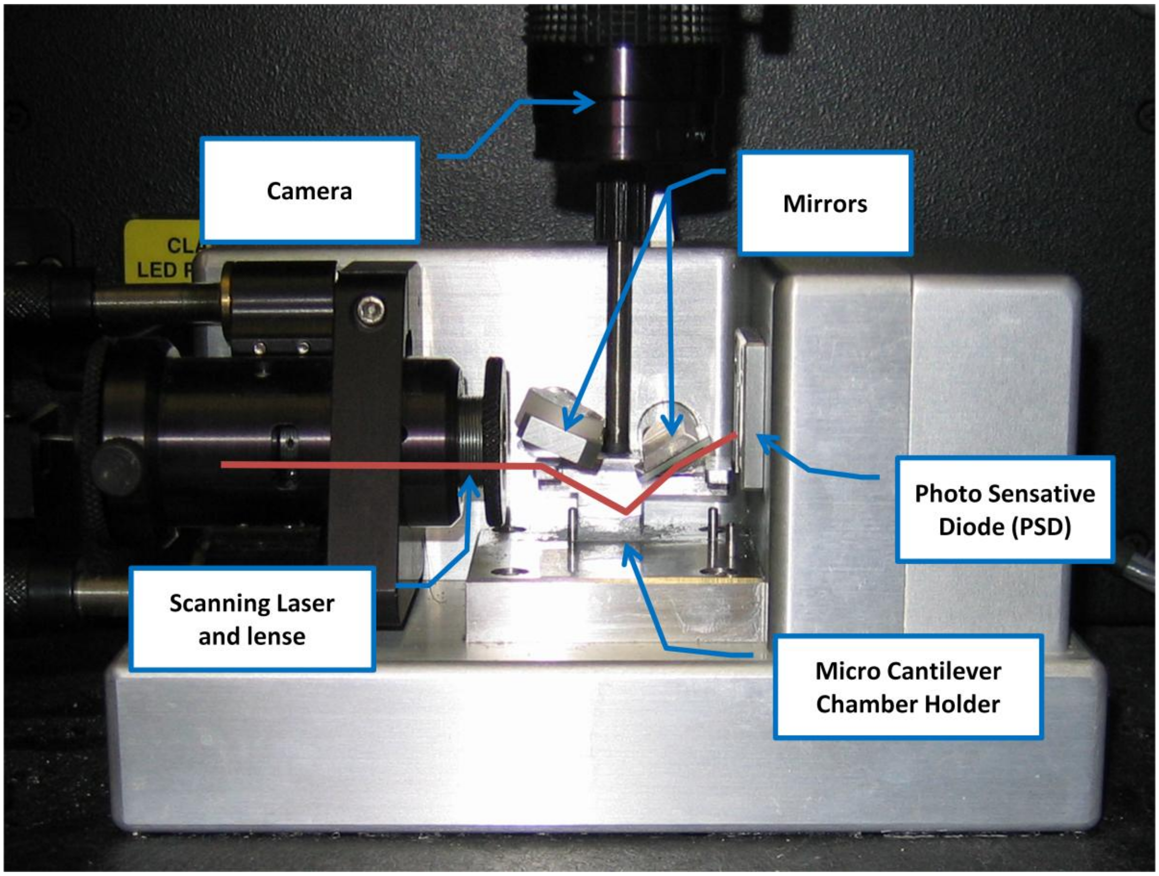

Figure 3.7 Sentris micro CSS utilizing a laser transduction method.

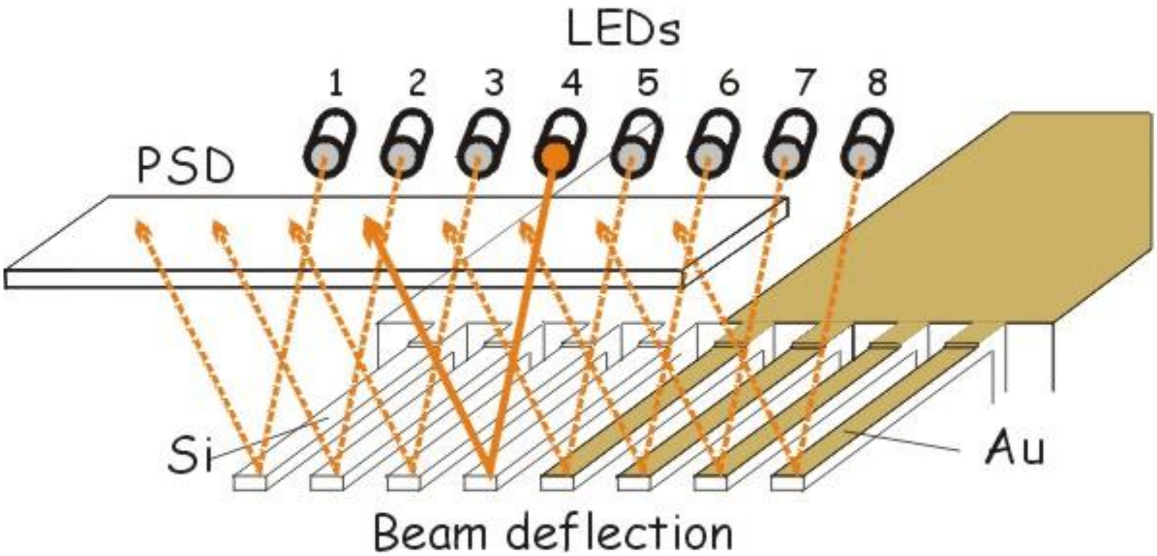

Figure 3.8 An illustrated cantilever array with optical transduction like that found in the Sentris apparatus [52]

Temperature is controlled by a resistance heater underneath the chamber and monitored by a thermocouple placed in the block. Due to the thermocouple measuring block temperature and not directly fluid temperature, some lag error was present. Using a second probe placed in fluid as illustrated in Figure 3.9, the thermal lag was found to be less than two degrees °C during temperature ramps.

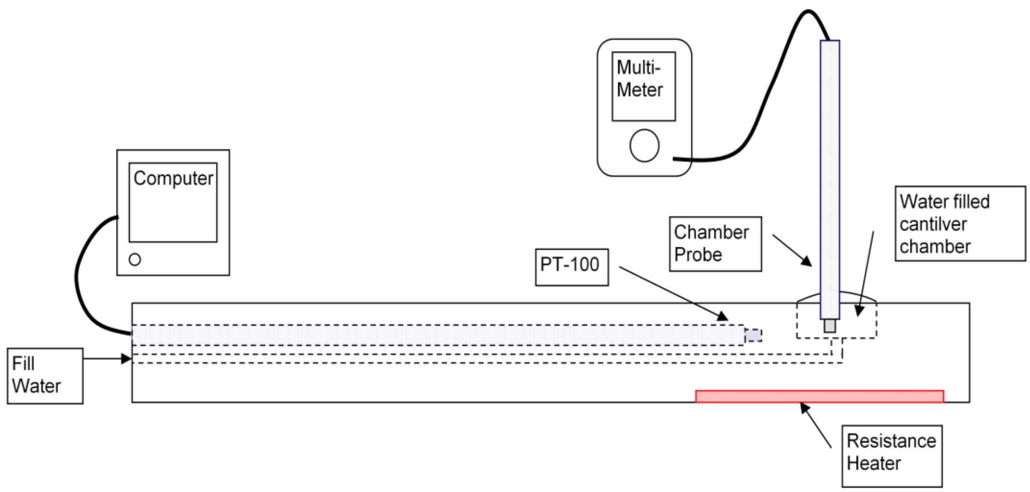

Figure 3.9 Thermally controllable microcantilever test chamber and test setup used test for presence of thermal lag.

As shown in Figure 3.8, the Sentris collects tip displacement data. The surface stress caused by test layer cannot be directly correlated to this tip displacement, due to polymers unknown physical properties. In order begin to understand the material properties of these thermally sensitive layers; a thin layer assumption was made. To correlate data back to a surface stress on the beams, the form of Stoney's equation previously discussed is used. Recalling Equation (2-4), we can use this equation as an approximate function of displacement *w* as shown in

$$\sigma_{st} = \frac{E t_s^2 w}{6 t_c L^2} \tag{3-1}$$

The modulus of elasticity (E) for silicon substrate was 112.4 GPa. The total length of the microcantilevers was 500 µm, however, due to laser focus being moved in from the tip slightly to facilitate a stronger signal the measured length (L) used was 450 µm and the cantilever thickness (t_s) of 1 µm. The film thicknesses (t_c) were not known to a high degree of certainty. However, for the purpose of calculations, the thickness the plasma polymer was set to the value found with the surface profiler of t_c=187 nm while the other configurations were set to an estimated thickness of t_c=7 nm.

In order to determine the effect solely of the surface stresses from polymer layers, other factors affecting the measurements are removed. As temperature increased, the aluminum chamber would expand causing a measured displacement change. This was corrected by the use of reference beams.

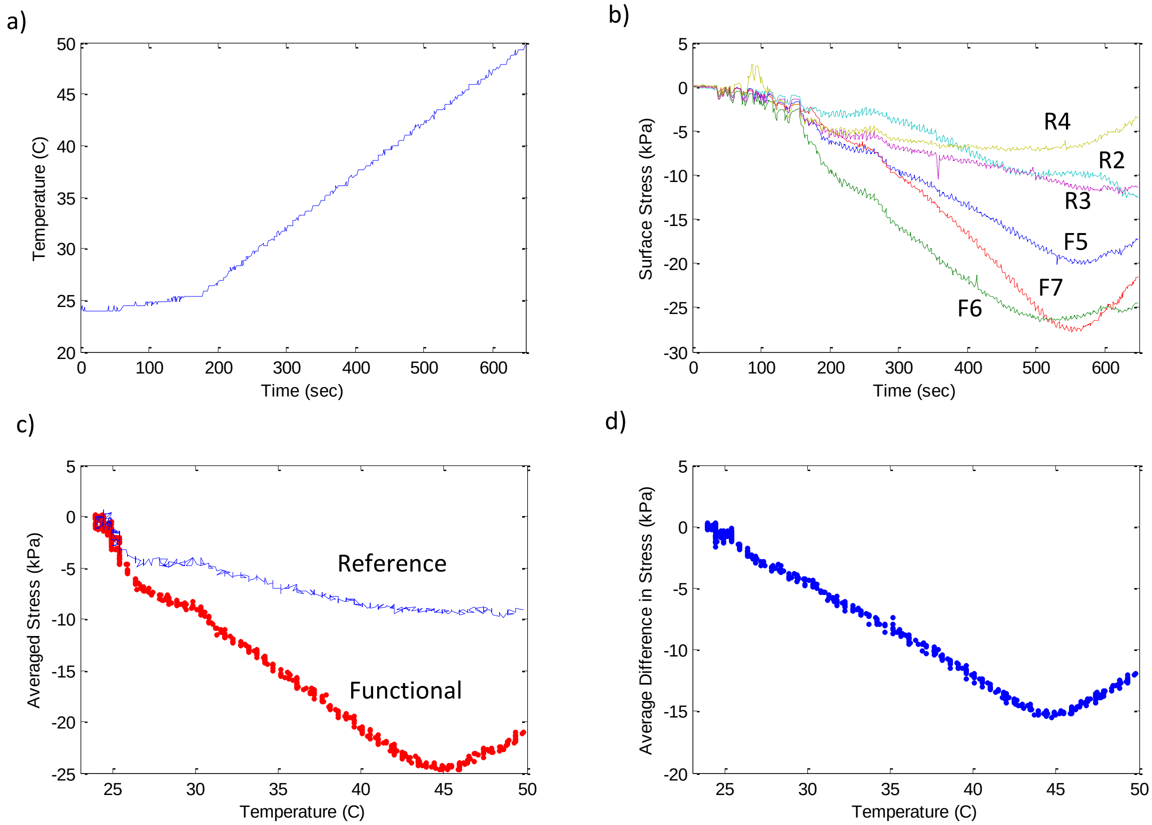

Figure 3.10 Constructing the stress change verses temperature. Positive values represent deflection away from functional surface. a) Chamber temperature is recorded with respect to time, b) while deflection data for functional cantilevers (F5-F7) and reference cantilever (R2-R4) is taken. c) Then, functional and reference tip deflection values are averaged and converted into stress, and finally d) the difference is taken resulting in deflection due to functionalization of cantilevers.

Stress data from the tested polymer was decoupled from other effects using reference cantilevers as shown in Figure 3.10. Low thickness of cantilevers caused insufficient laser signal strength on certain cantilevers in which case said cantilever were discounted. Results are averaged and show repeatability as seen in Figure 3.11.

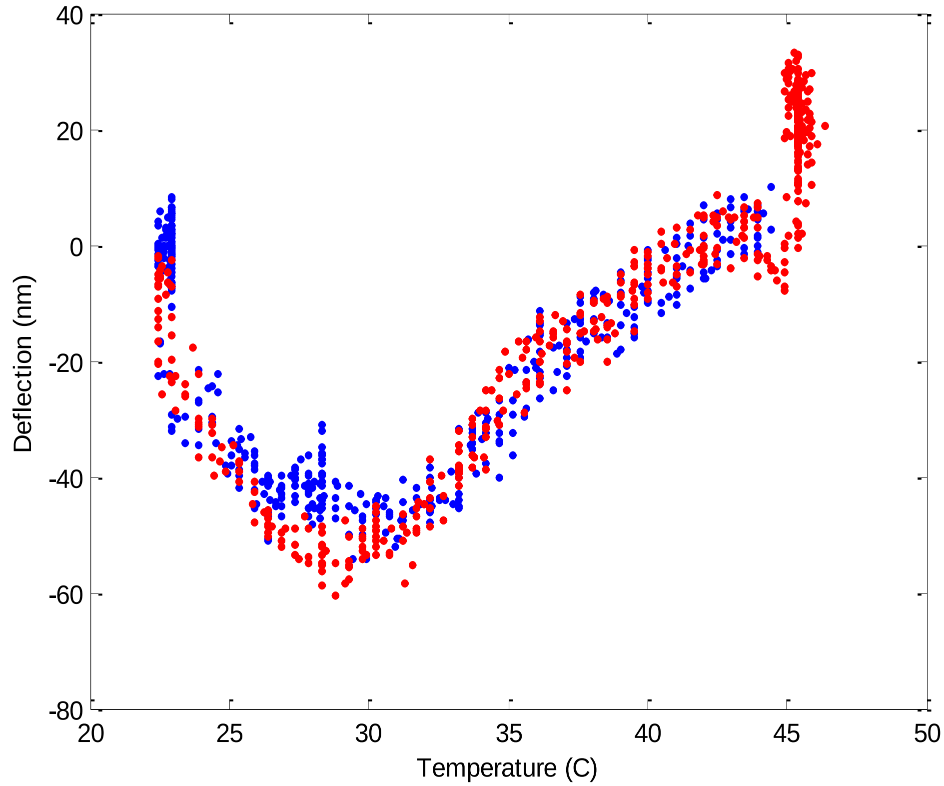

Figure 3.11 Repeated overlaid tests of deflection of cantilever due to PNIPAM in polymer brush configuration demonstrating excellent repeatability.

Results and Discussion

From these test results the stresses caused during the transition through the LCST is observed. As shown in Figure 3.12, the effects of the transition through the LCST can be observed by the mechanical stresses caused by the polymer on the microcantilever. This represents a novel method for determining the LCST.

At the LCST, the layer of thermally sensitive polymer will be completely dehydrated and further increase of temperature will not show effect of film collapse. If sufficient grafting density is present, the effect from a bi-material with different thermal expansion coefficients will still be present. Because the polymer has a much higher thermal coefficient of expansion than of the silicon, the stress this causes will have an opposite sign than that of the dehydration effect. The LCST is then the point where the stress from dehydration stops.

Two variations on the polymer brush were tested demonstrating similar behavior. As temperature increases from room temperature, dehydration occurs as intermolecular bonding within the chain becomes more favorable. This causes the swollen layers to collapse as they dehydrate, creating a negative stress and causing the cantilever to bend towards the functional side. At the LCST, the layer becomes completely dehydrated. At this point the surface property of the polymer changes from hydrophilic to hydrophobic as seen from contact angle tests Figure 3.2. After dehydration, the difference between thermal expansion of the polymer and silicon become the only effect from the polymer causing a positive stress on the cantilever. The result is a change in the rate of change of stress versus temperature. For both polymers, this occurs at a temperature of 32 °C. The temperature may be slightly high due to some lag in the temperature measurements which from testing could be as great as 2 °C.

Depositions of the plasma polymer resulted in the thickest polymer layers. Effects are quite similar. The observed LCST is seen to occur at a higher temperature of about 44 °C. Due to the thickness of the layer and higher displacements, results are well defined. Due to weaker bonding with the cantilever, repeated tests on the same set of cantilevers results in degrading responses when repeated. However, the results with newly deposited polymer were consistent.

For the case of the grafted to polymer, it was theorized that grafting density would play a significant role in the stress transferred to the cantilever. The polymer was known to have a significantly lower level of grafting density and also lacked the cross linking that the plasma polymer had. As shown in Figure 3.12, the presence of a LCST cannot be observed utilizing this method.

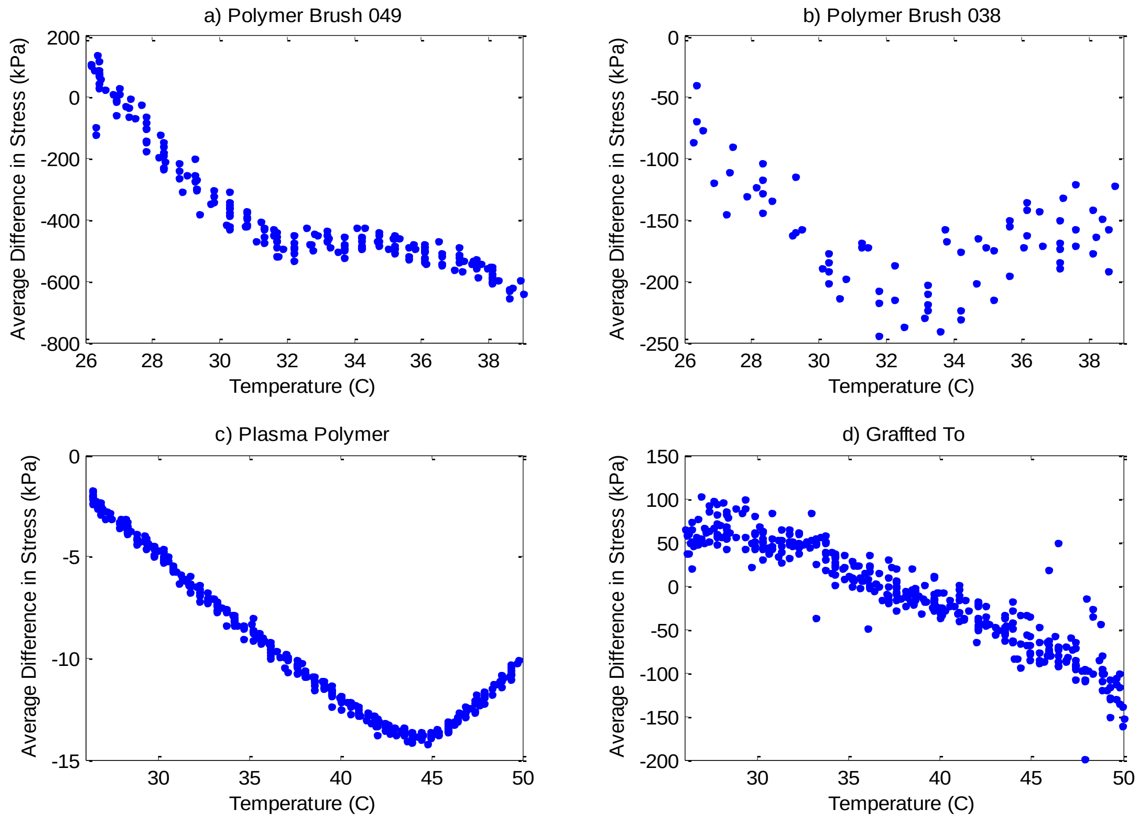

Figure 3.12 Deflection of cantilever due to PNIPAM for a) short coils cantilever chip #049, b) cantilever chip #038 with long coils, c) and plasma deposited polymer shows initial bending due to water dehydration followed by bimaterial effect. Shorter coils result in less biomaterial effect. No significant effect is seen by d) low grafting density grafted to polymer. Data not corrected for temperature lag.

Summary

In this chapter, it was shown that utilizing a CSS to measure the surface stress of a polymer can be used to determine the LCST for different types of thermally sensitive polymers. This temperature was shown as the point where negative surface stress from layer dehydration stops as temperature is increased causing a change in rate of deflection versus temperature. The CSS method allows for a temperature sweep instead discrete contact angle measurements. When grafting to polymer that had a low grafting density was tested, the polymer did not create sufficient surface stresses for this method to effectively determine LCST. Therefore when utilizing CSS it confirmed that grafting density is a limiting factor.

CHAPTER 4 : GOLD NANOPARTICLE MASS DETECTION USING DYNAMICS MODE CSS WITH NOVEL INTEGRATED GAUGE READOUT

Motivation

In past works, most transduction of the mechanical movement has been performed using optical detection methods, which are not ideal for inexpensive and compact systems as complexity increases. The new systems may consist of large arrays of cantilever devices. These would include a multitude of both functional and reference elements. Because of the large number of signals, there are significant drawbacks to optical transduction techniques. These include difficulty in focusing a multitude of lasers on cantilevers and the cost and bulkiness of the off chip laser and PSD. Integrated readout has been achieved by integration of piezoresistive layers into the mechanical devices [53]. The choice material for the piezoresistive layer is usually poly or single crystal silicon, due to its tunable and high gauge factor. However, the electrical signal is plagued by high Johnson and flicker noise, which limits the signal to noise ratio. Furthermore, the fabrication of silicon based piezoresistors consists of several expensive depositions, doping and annealing steps, which are undesirable with respect to cost and thermal budget. It has been shown that Au can also be used instead of a piezoresistive layer [54, 55]. Even though the gauge factor is low (K~2-5), the electrical noise compared to silicon based resistors is much lower, thus the signal to noise ratio is comparable if not better than silicon based piezoresistive readout, especially when scaling down the size of the mechanical sensor. This chapter presents the fabrication and characterization of a micro CSS with an integrated Au strain gauge readout.

Fabrication of micro CSS with integrate gauge readout

A simple, two-mask fabrication has been used to realize silicon nitride nanomechanical devices, with integrated Au strain gauge readout. By exchanging doped silicon with Au, the time, cost and complexity of fabrication are lowered substantially.

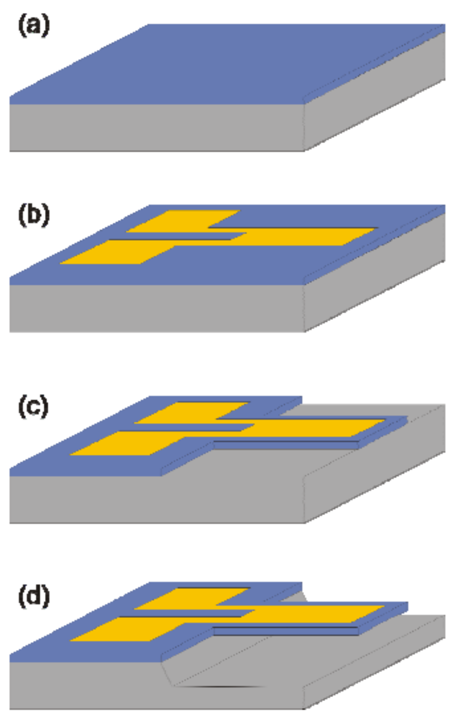

Figure 4.1 The fabrication process for resistance readout based CSS.

Figure 4.1 schematically depicts the fabrication process. First, a 500nm thick silicon nitride layer is deposited using a low stress and low temperature PECVD process. Then, using positive photolithography to protect cantilever geometry, the undesired silicon nitride is removed via reactive ion etching. This step defines the cantilever shape with the results seen in Figure 4.2

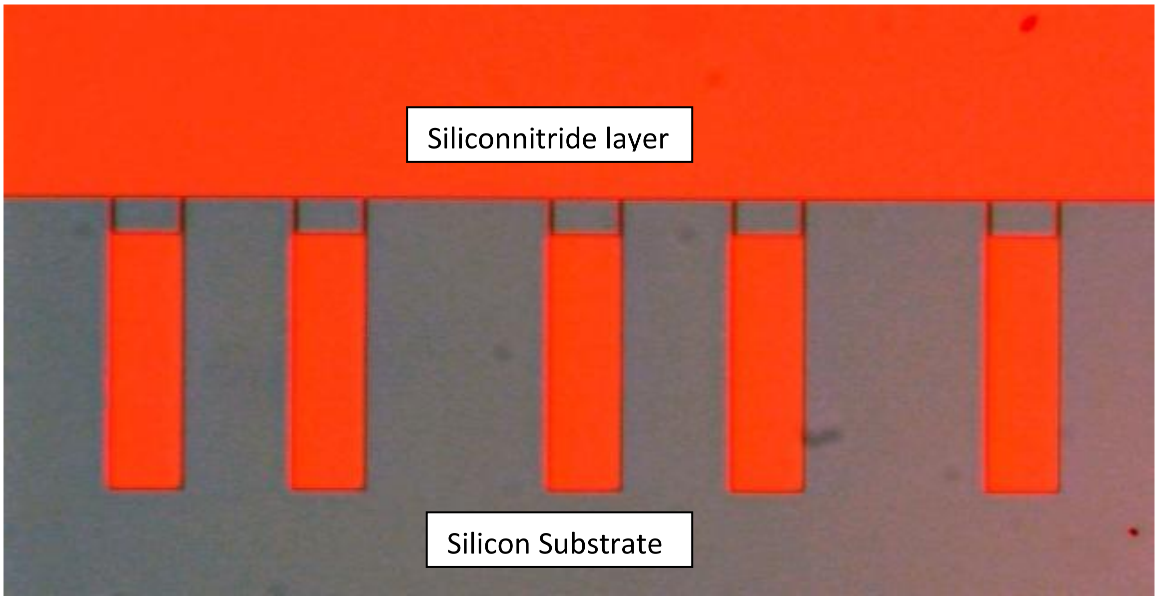

Figure 4.2 Silicon nitride cantilever outline that is grown from silicon wafer with geometry defined by photolithography.

Following this, a negative photolithography is used to expose only gauge areas. Then, a 10-20nm thick Au layer is deposited. The Au that is deposited on top of the photoresist is then removed using a lift-off technique resulting in the desired Au strain gauge pattern. This is repeated to provide a thicker Au layer where wire bonding will be required. Results from this step are shown in Figure 4.3.

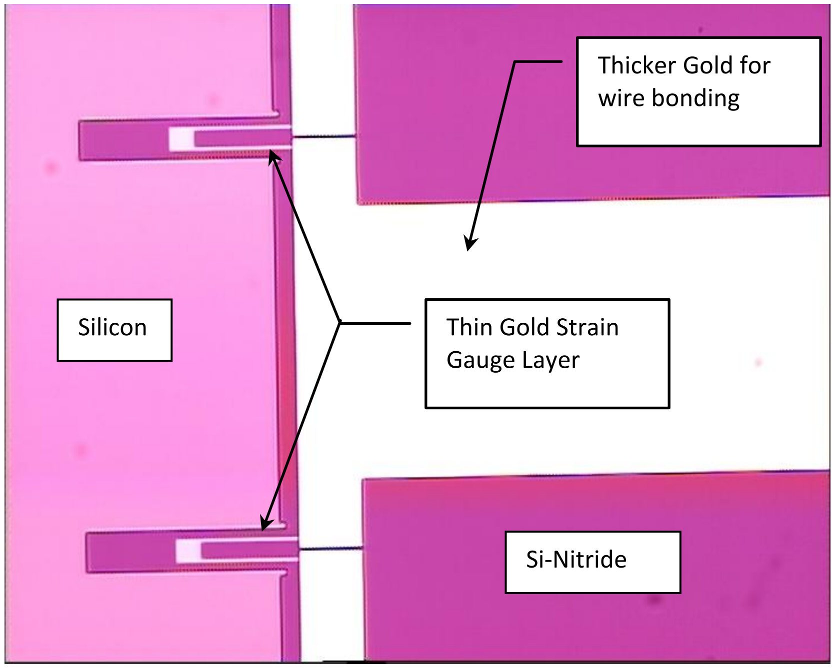

Figure 4.3 Silicon nitride microcantilever outline with Au strain gauges deposited. A thin layer is deposited on the cantilever itself while to the right of the image is the thicker layer necessary for wire bonding.

Finally, the structures are under etched using KOH etching, where no backside protection is needed. An SEM image of the under etched cantilever device can be seen in Figure 4.4.

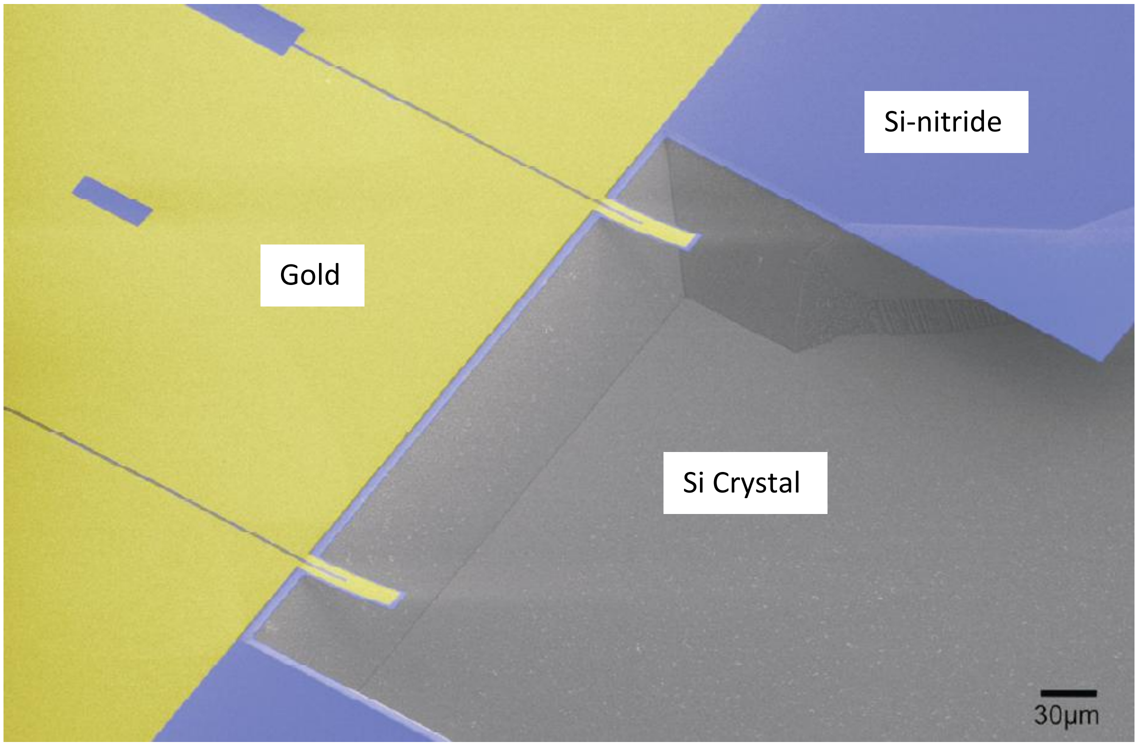

Figure 4.4 An SEM image of fabricated cantilevers with gold layer atop the layer of the Si-nitride overhanging an etched pit of silicon crystal.

One major advantage with this process sequence compared to other works is the fact that the PECVD nitride has extremely good mechanical properties and can still be deposited at low temperature. Thus, encapsulation of the Au resistors is possible by adding an extra PECVD nitride layer on top of the Au layer, prior to the RIE etch. This would make it possible for operation in liquids.

Results and Discussion

The dynamic properties of the device were investigated by actuating with a piezo-element mounted underneath the device and the readout of the movement is performed by using a Wheatstone bridge configuration, where two device resistors and two off chip variable resistors were used as illustrated in Figure 4.5

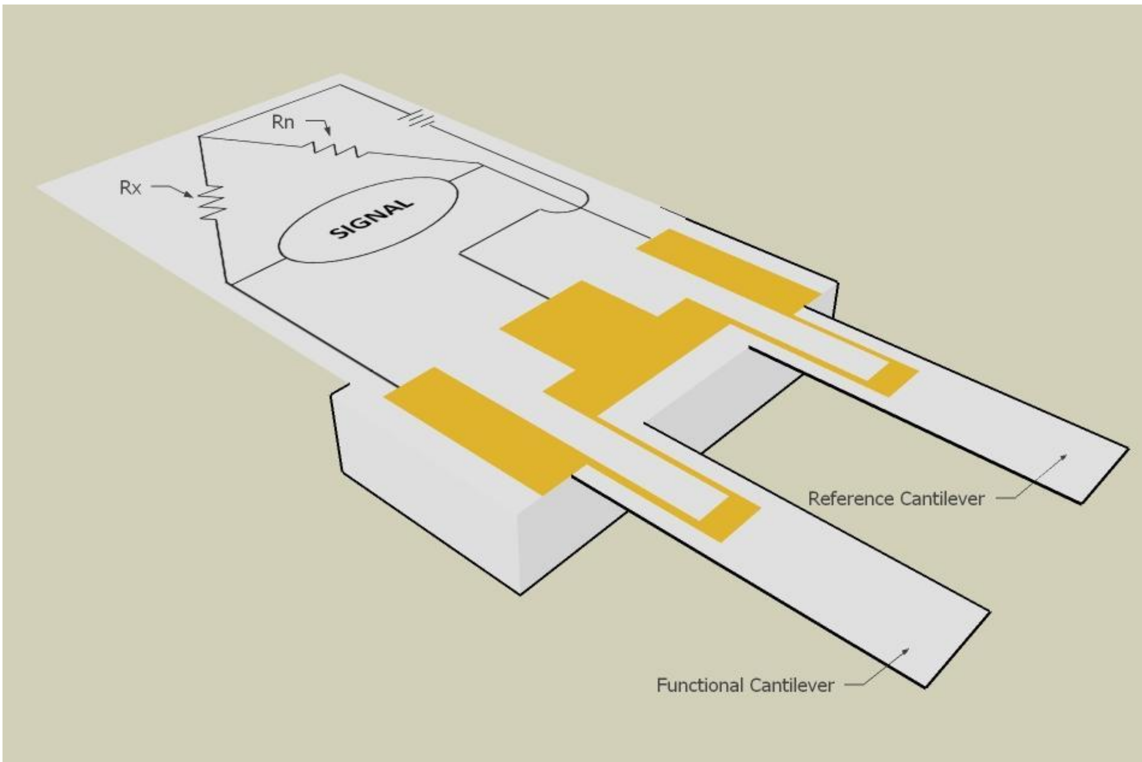

Figure 4.5 Dual CSS with integrated gauge readout using a Wheatstone bridge circuit.

The Dual CSS is then placed in a vacuum chamber that is evacuated to an absolute pressure of 2Pa in order to improve the Q-factor. The approximate resonant frequency is obtained utilizing a laser-based transduction method. This showed agreement with latter results.

The voltage output versus the actuation frequency is shown in Figure 4.6 for the 1st mode of a cantilever device with dimensions 150µm x 30µm x 500nm. Initially, there is a slight miss-balance in the Wheatstone bridge, due to insufficient tuning ability in variable resistors R_x and R_n. In the frequency response plot, there is a peak and negative peak, corresponding to cantilevers 2 and 1. When cantilever 1 resonates, the Wheatstone bridge is being balanced and shows a negative peak response. Conversely, when cantilever 2 resonates bridge imbalance is increased and shows the peak response.

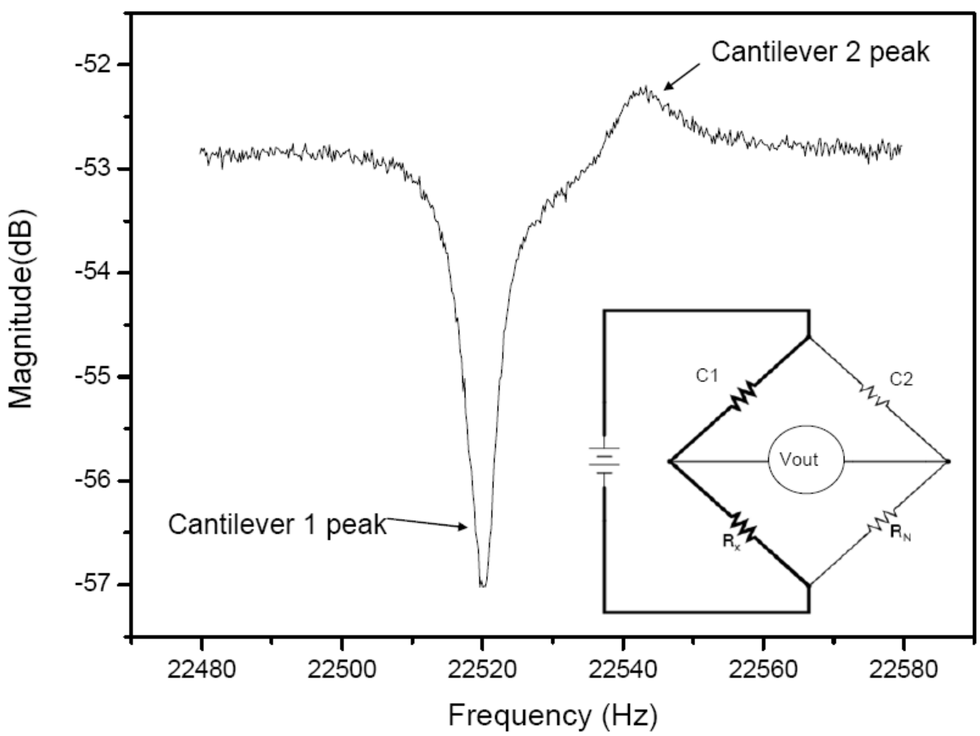

Figure 4.6 Frequency response of two CSS showing two resonance frequencies correlating to each cantilever's first eigenfrequency. The inserted plot is the Wheatstone bridge setup used to measure the output.

The calculated Q-factor at 2Pa is between 2000-3000 for the largest resonance peak. The reason for the low peak size for cantilever 2 is not certain, but could be due to damage on the Au resistor. This is, however, not normal and has only been seen on this device. In order to test the mass sensitivity of the cantilever, controlled deposition of Au nanoparticles were used.

The Au nanoparticles were fabricated using a known colloidal chemistry technique [56]. These resulted in particles with a theoretical size of 45 nm. This was verified utilizing an SEM shown in Figure 4.7.

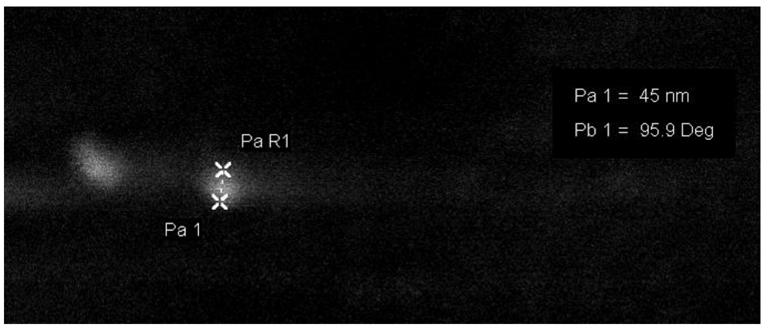

Figure 4.7 Au nanoparticles under very high resolution from an SEM showing an approximate diameter of 45 nm.

The nanoparticles are then deposited on one of the cantilevers by spotting a small amount of nanoparticle suspension utilizing a nanospotter. The device is then brought directly back into the vacuum chamber for measurements.

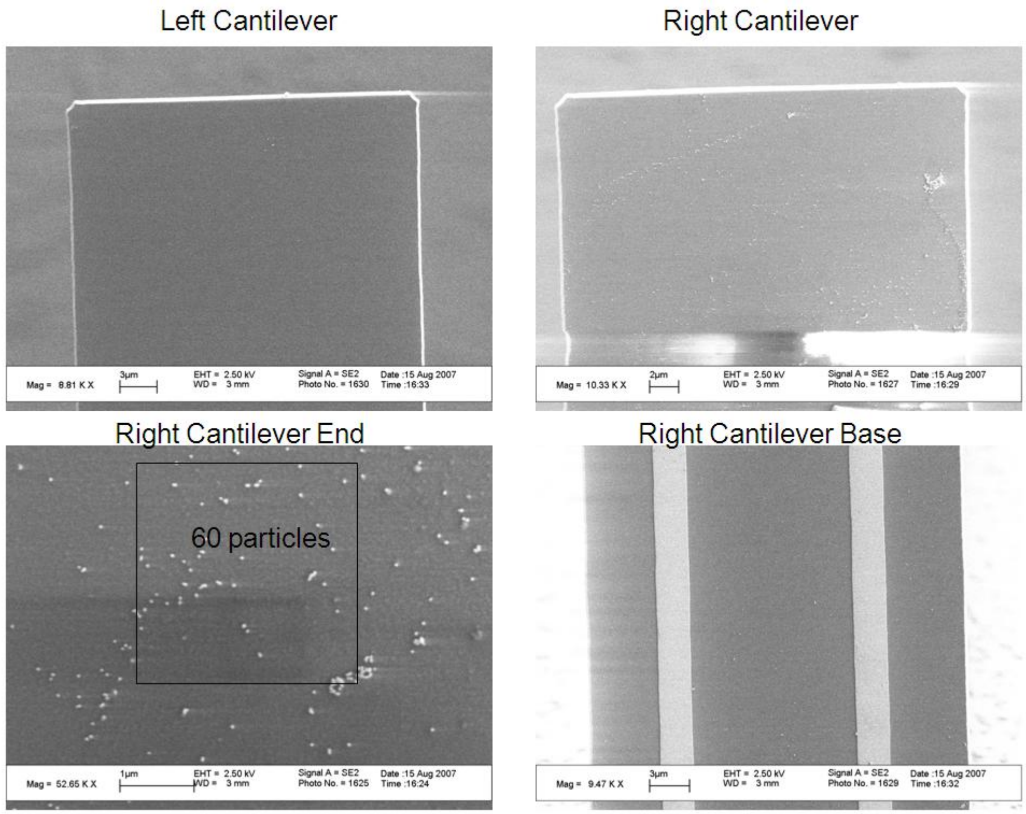

Figure 4.8 SEM images of cantilever with deposited 45nm Au nanoparticles and reference cantilever. As shown, such imagines quantify the number of nanoparticles on surface possible.

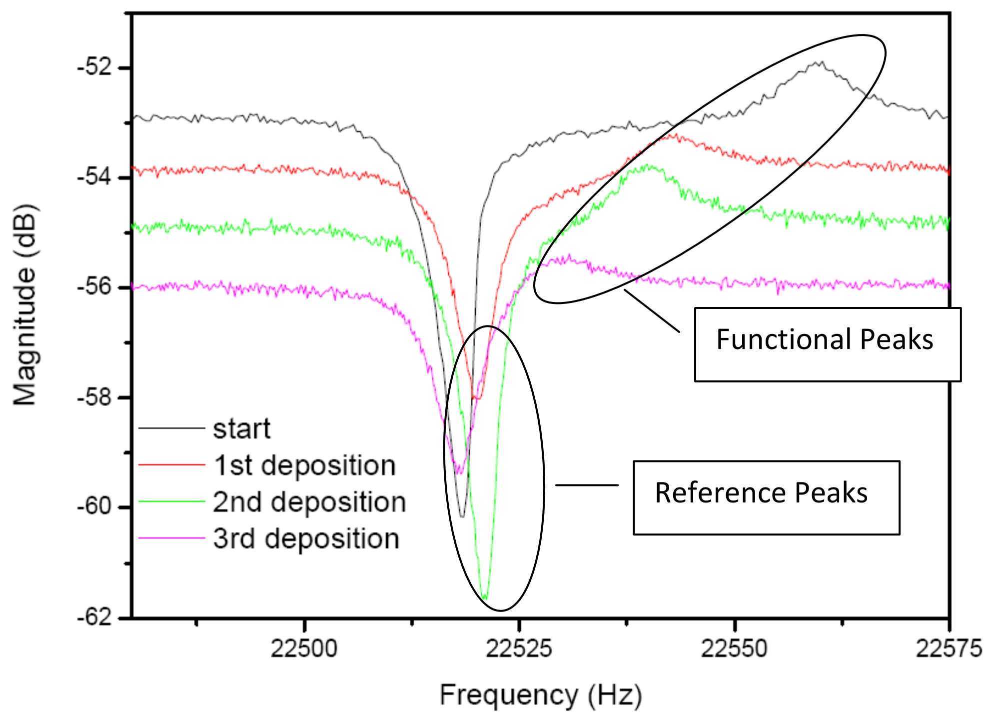

Figure 4.9 Frequency response signal for dual cantilever with integrated strain gauge after repeated depositions of Au nanoparticles with DC offsets added to ease viewing.

The frequency response of the device is plotted before and after three subsequent depositions in Figure 4.9. It is shown that the large left peak seems relatively unchanged while the small right peak shifts downwards, due to the added Au nanoparticle mass. In Figure 4.8, the difference in resonant frequency of cantilevers 2 and 1 is shown, the decreasing gap due to the decreasing resonant frequency of cantilever 2. By measuring the difference between the two peaks, fluctuations of the cantilever resonance frequency due to temperature and/or pressure changes can be filtered out, thereby making the technique very accurate. By SEM imaging the surface, the approximate number of particles per deposition has been calculated to 1500, which corresponds to an added mass of approximately 1.5pg. The mass sensitivity of the used device is estimated to approximately 130fg/Hz, thus 260pg is expected to give a frequency shift of 12Hz, which is good correspondence to Figure 4.10.

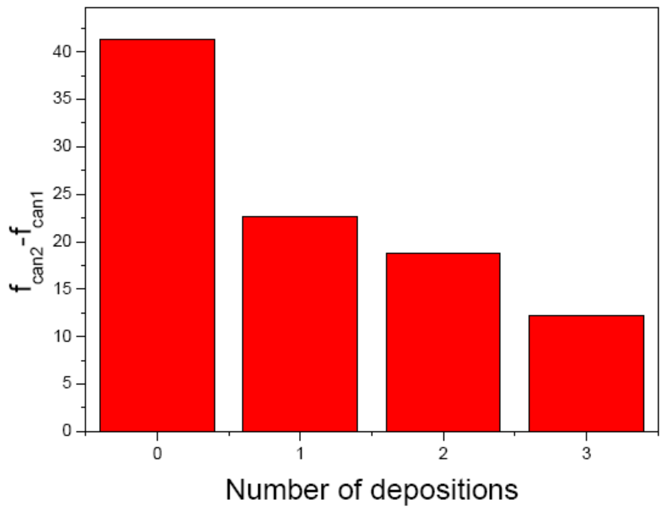

Figure 4.10 The difference between resonant frequencies of the two cantilevers after nanoparticle depositions.

This method for characterization of sensitivity by obtaining average particle can become an effect tool. One potential obstacle yet to be overcome in order to achieve better verification is that no particles are collected on underside of cantilever. If this can be verified, the average number of particles that are collected per deposition can be found in an independent experiment. Conducting a particle count after each deposition is not practical due to extended time to obtain SEM image and is not as accurate due to mass deposition during SEM process. This process would eliminate the need for SEM verification.

Summary

This chapter has covered the fabrication and testing of a new cantilever design with a transduction method utilizing an integrated strain gauge. This advancement resolves some of the issues with optical transduction methods by decreasing the size and cost of apparatus while still correcting for environmental effects. These new cantilevers were tested using the second operational mode for CSS to detect the presents of Au nanoparticles.

CHAPTER 5 : SENSITIVITY ENHANCEMENT OF CSS USING DELAYED FEEDBACK

Introduction and Sensitivity Background

Sensitivity constitutes one of the most desirable characteristics of CSS. For instance, sensing of chemical reagents requires selective detection of masses in the order of sub-nanograms. Otherwise, the concentration of these compounds in the environment can reach hazardous levels. Unfortunately, sensitivity of current CSS is predominantly limited by their size. As a result, accurate detection of smaller masses or stresses requires the fabrication of ultra-small sensors. This, however, can be a formidable task and significantly increases the effect of noise on the sensor measurements. Moreover, in many applications, the sensor must operate in air or water where damping is relatively large and the quality factor (Q) can be very small [57]. For small Q, the sensor cannot detect small changes in mass/stress because of its inability to resolve small frequency shifts. This directed the research towards creating new methodologies for ultra-sensitive sensing [58, 59, 60].

Along this line of reasoning, we propose a simple, but effective concept to enhance the sensitivity of CSS. This novel methodology is based on utilizing feedback delays and inherent system nonlinearities to create a limit-cycle type response whose amplitude is ultra-sensitive to frequency variations. Feedback delays are usually associated with instabilities because they inadvertently channel energy into or out of systems at improper time intervals [61, 62, 63]; our principle of ultra-sensitive sensing builds on these instabilities. More importantly, the proposed methodology does not require any changes or additions to the current sensor geometry or design, and can be implemented in real-time and on any of the previously discussed transduction methods. Using this approach, we can also incorporate any system delays into the parametric delay which we deliberately introduced for the purpose of sensitivity enhancement.

Effect of Feedback Delays on the Dynamics of Cantilever Beams

In order to demonstrate the proposed concept, we first analyze the effect of time-delays on the linear and nonlinear stability of the cantilever response. More specifically, we illustrate how linear feedback delays combined with inherent system nonlinearities can produce stable limit cycles that have amplitudes that are ultrasensitive to frequency variations and hence can be effectively utilized for sensitivity enhancement.

Beam Modeling

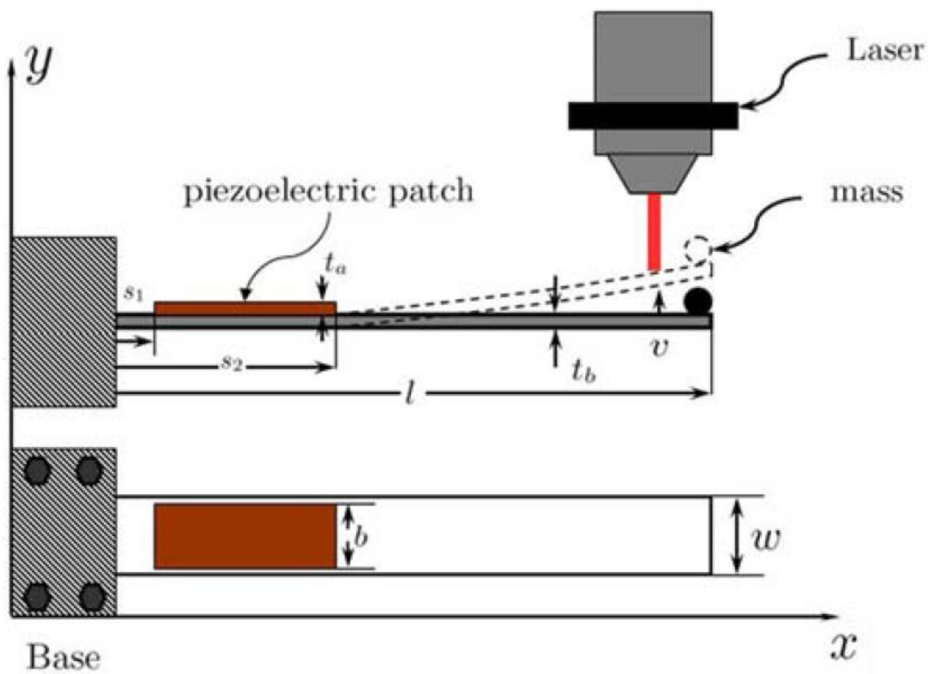

Figure 5.1 CSS setup with piezoelectric patch actuation. This is a common setup on both macro and micro CSS.

We consider an isotropic inextensible Euler-Bernoulli cantilever beam excited by a piezoelectric patch using a delayed position feedback signal as illustrated in Figure 5.1. When only planar motions are considered, a reduced-order model describing the nonlinear response of the first-mode beam vibrations can be written as:

$$\ddot{v} + \mu\dot{v} + \omega_n^2 v = \Gamma v^3 + 2\Lambda(v^2\ddot{v} + \dot{v}^2 v) + Gv(t-\tau) \qquad \textbf{(5-1)}$$

where the dots indicate derivatives with respect to the time t, v is a generalized temporal coordinate representing the deflection of the beam, μ is a modal damping term, t is a feedback delay, and

$$\omega_n^2 = \frac{EI}{\rho A} r_n^4, \qquad \Gamma = \frac{EI}{\rho A} \int_0^l (\phi_1')^2 ((\phi_1'')^2 + \phi_1' \phi_1''') ds,$$

$$\Lambda = -\frac{1}{2} \int_0^l \left(\int_0^s (\phi_1')^2 ds \right)^2 ds, \tag{5-2}$$

$$G = -\frac{kbd_{31} E_a (t_a + t_b)}{\rho A} [\phi_1'(s_2) - \phi_1'(s_1)].$$

Here, the primes indicate derivatives with respect to the arclength s, ρ is the beam density, A is the beam cross-sectional area, E is the Young's modulus of elasticity of the beam, I is the moment of inertia about the neutral axis of the beam, L and t_b are the beam length and thickness, respectively, b and t_a are the width and thickness of the piezoelectric patch, respectively, d_{31} is the electromechanical coupling coefficient, E_a is the piezoelectric material Young's modulus, s_1 and s_2 are, respectively, the starting and ending coordinates of the piezoelectric strip, k is the feedback gain, ϕ_1 is the spatial variation of the first vibration mode, and r_n can be obtained using the following characteristic equation,

$$\begin{aligned} &-\cos \mathrm{r_n l} - \cosh r_n l - \Pi(\sin r_n l - \sinh r_n l) \\ &+ \frac{M}{\rho A l} r_n \big(\sin r_n l - \sinh r_n l - \Pi(\cos r_n l - \cosh r_n l)\big) = 0, \end{aligned} \tag{5-3}$$

where $\Pi = \frac{\sin r_n l + \sinh r_n l}{\cos r_n l + \cosh r_n l}$

with M denoting the added mass. For more details on the derivation, we refer the reader to [64]. It is worth noting that, when a mass M is added to the tip of the cantilever beam, the frequency ω_n, mode shape ϕ_1, and the other nonlinear coefficients vary significantly. However, when M is very small compared to the mass of the beam (i.e., $M \ll \rho AL$), the effect of the mass on the nonlinear coefficients is minimal and therefore can be neglected.

Linear Stability Analysis

We begin with a detailed linear stability analysis of the response of a cantilever beam experiencing delayed-position feedback. As such, we retain only the linear terms in Equation (5-1), and, for simplicity, let $G = K\omega_n^2$ to obtain

$$\ddot{v} + \mu\dot{v} + \omega_n^2 v = K\omega_n^2 v(t-\tau) \qquad \textbf{(5-4)}$$

To characterize the stability of Equation (5-4), one can use traditional frequency-domain techniques or assume a temporal steady-state response of the form [65, 66]

$$v = Ae^{\sigma t}\cos(\omega t + \theta) \qquad \textbf{(5-5)}$$

where A is the oscillation amplitude, σ is a damping parameter, ω is the frequency of the delayed response, and θ is a constant phase angle. Substituting Equation (5-5) into Equation (5-4) and setting the coefficients of $\sin(\omega t + \theta)$ and $\cos(\omega t + \theta)$ equal to zero independently yields

$$\lambda(2\zeta + v)e^{2\pi\zeta\gamma} + K\sin(2\pi\lambda\gamma) = 0 \qquad \textbf{(5-6)}$$

$$(\lambda^2 - \zeta^2 - v\zeta - 1)e^{2\pi\zeta\gamma} + K\cos(2\pi\lambda\gamma) = 0 \qquad \textbf{(5-7)}$$

where $\lambda = \frac{\omega}{\omega_n}, \zeta = \frac{\sigma}{\omega_n}, v = \frac{\mu}{\omega_n}, \gamma = \frac{\tau}{T}, \text{and } T = \frac{2\pi}{\omega_n}$. The stability of the system is determined by the value of the damping parameter, ζ. The system is asymptotically stable when $\zeta < 0$ and unstable when $\zeta > 0$. To obtain the boundaries of stability, we set $\zeta = 0$ in Equation (2-19) and Equation (5-7) and solve the resulting equations for γ and *K* to obtain

$$\gamma_{cr} = \frac{1}{2\pi\gamma_{cr}}\left(\tan^{-1}\frac{\lambda_{cr}v}{\lambda_{cr}^2 - 1} + n\pi\right), \qquad n = 0,1,2,\ldots \qquad \textbf{(5-8)}$$

$$K_{cr} = \pm\frac{\sqrt{\lambda_{cr}^2 v^2 + \lambda_{cr}^4 - 2\lambda_{cr}^2 + 1}}{\lambda_{cr}^2} \qquad \textbf{(5-9)}$$

where K_{cr}, γ_{cr}, and λ_{cr} represent the gain, dimensionless delay, and dimensionless delayed-frequency at the stability boundary, respectively. Equation (5-8) and Equation (5-9) are utilized to construct a stability diagram for the trivial solutions of Equation (5-4) as illustrated in Figure 5.2. The shaded regions represent gain-delay combinations leading to asymptotically stable solutions while the un-shaded areas represent combinations leading to linearly unstable cantilever response.

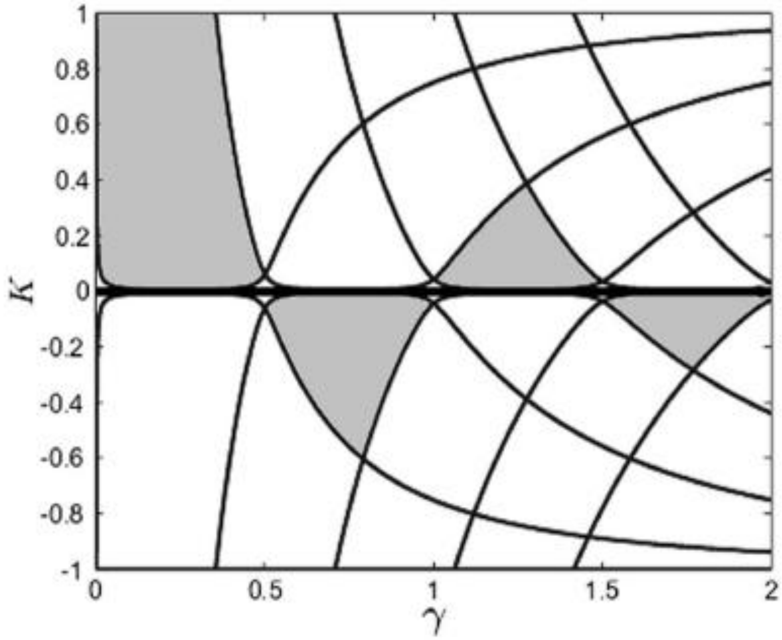

Figure 5.2 Stability pockets of Equation (5-4). Shaded regions represent gain-delay combination leading to asymptotically stable cantilever response. This chart was obtained for v=0.006 [67].

Nonlinear Stability Analysis

Linear theory is capable of determining regions wherein small motions become dynamically unstable and predicts that unstable solutions grow without bound. However, as the amplitude of motion grows, the nonlinearity plays an important role in limiting the growth resulting in nontrivial solutions. These solutions can be stable or unstable depending on the nature of the bifurcation at the stability boundary.

Bifurcation Normal Form

The nature and stability of the beam response very close, but outside the shaded regions depicted in Figure 5.2, is determined by obtaining the normal form of the bifurcation. In other words, we examine the response behavior upon crossing these stability boundaries. This is accomplished by increasing either K or γ beyond the critical values defined in Equations (5-8) and (5-9). Different approaches can be followed to construct the normal form of the bifurcation for time-delay systems. Examples include the method of multiple scales [68, 69], the center manifold reduction [64], and the iterative perturbation technique [70].

Multiple Scales Solution

Due to the nonlinearity of the problem, traditional methods of solving the problem are ineffective. The method of multiple scales is used to obtain the modulation equations. Choosing three time scales results in a solution in the form of.

$$v(t) = v_0(t) + \epsilon\, v_1(t) + \epsilon^2 v_2(t) \quad \textbf{(5-10)}$$

$$t = T_0 + \epsilon T_1 + \epsilon^2 T_2 \quad \textbf{(5-11)}$$

For these time scales the first and second time derivatives then become;

$$\frac{d}{dt} = D_0 + \epsilon D_1 + \epsilon^2 D_2 \quad \textbf{(5-12)}$$

$$\frac{d^2}{dt^2} = D_0^2 + 2\epsilon D_0 D_1 + \epsilon^2 (D_1^2 + 2D_0 D_2) \quad \textbf{(5-13)}$$

Where D_x represents the derivative with respect to the x^{th} time scale. To indicate how far over the linear stability boundary the operating point is, the gain K is defined as $K_c + \epsilon K_2$ where K_c represents the critical gain that lies on the stability boundary defined by Equations (5-8) and (5-9) and K_2 is the variation away from this point. The various parameters are scaled to appropriate time scales.

$$K = K_c + \epsilon K_2 \tag{5-14}$$

$$\Gamma = \epsilon^2 \Gamma \tag{5-15}$$

$$\Lambda = \epsilon^2 \Lambda \tag{5-16}$$

Taking these definitions and substituting them back into Equation (5-1) and collecting the orders of ϵ yields.

$$O(\epsilon^0) \rightarrow D_0^2 v_0 + 2\mu D_0 v_0 + \omega n^2 v_0 + K_c D_0^2 v_0(t-\tau\,) = 0 \tag{5-17}$$

$$\begin{aligned} O(\epsilon^1) \rightarrow\; & \omega^2 v_1 + 2\mu D_0 v_1 + 2\mu D_1 v_0 + D_0^2 v_1 + 2D_0 D_1 v_0 \\ & + K_c\; D_0^2 v_1(t-\tau) + \left(2K_c D_0\; D_1 + K_2\; D_0^2\right) v_0 = 0 \end{aligned} \tag{5-18}$$

$$\begin{aligned} O(\epsilon^2) \rightarrow\; & D_0^2 v_2 + 2D_0 D_1 v_1 + \left(D_1^2 + 2D_{0D_2}\right) v_0 + 2\mu\; D_0 v_2 + 2\mu D_1 v_1 \\ & + 2\mu D_2 v_0 + \omega n^2 v_2 + K_c D_0^2 v_2(t-\tau) + 2K_c D_0 D_1 v_1(t-\tau) \\ & + (K_c(D_1^2 + 2D_0 D_2) + K_2 D_0^2) v_0(t-\tau) - \Gamma v_0^3 - 2\beta\Lambda D_0^2 v_0 \\ & + 2\Lambda\; v_0 D_0 v_0^2 \end{aligned} \tag{5-19}$$

From $O(\epsilon^1)$ equation we find that the system has a solution in the form.

$$v_0 = A(T_1, T_2) e^{i\omega T_0} + \bar{A}(T_1, T_2) e_0^{-i\omega T} \tag{5-20}$$

Substituting (5-20) into the $O(\epsilon^1)$ (Equation (5-18)) expression and eliminating secular terms shows that A is a function of T_2 solving for v_1 and substituting back into $O(\epsilon^2)$. Eliminating secular terms yields the following modulation equations.

$$\dot{a} = \frac{1}{v^2 + 4\gamma_{cr}^2}\left(K_2\omega_n H_1 a + \frac{1}{4\omega_n} N_{eff} v a^3\right) \quad \textbf{(5-21)}$$

$$a\dot{\beta} = \frac{1}{v^2 + 4\gamma_{cr}^2}\left(K_2\omega_n H_2 a + \frac{1}{2\omega_n} N_{eff} \lambda_{cr} a^3\right) \quad \textbf{(5-22)}$$

where *a* and β are the amplitude and phase of the response, respectively, $K_2 = K\text{-}K_{cr}$, and

$$H_1 = v\cos(2\pi\lambda_{cr}\gamma_{cr}) - 2\sin(2\pi\lambda_{cr}\gamma_{cr})\lambda_{cr} \quad \textbf{(5-23)}$$

$$H_2 = v\sin(2\pi\lambda_{cr}\gamma_{cr}) + 2\sin(2\pi\lambda_{cr}\gamma_{cr})\lambda_{cr} \quad \textbf{(5-24)}$$

$$N_{eff} = 4\Lambda\lambda_{\mathrm{cr}}^2\omega_{\mathrm{n}}^2 - 3\Gamma \quad \textbf{(5-25)}$$

Equations (5-21) and (5-22) represent the normal form for a Hopf bifurcation of a fixed point. The nature of the Hopf bifurcation is determined by the sign of K_2, H_1, and N_{eff} (*the effective nonlinearity coefficient*). Using Equation (5-8) and Equation (5-9), it is not difficult to show that, for positive values of K_{cr}, H_1 is always negative. By choosing K_2 as a bifurcation parameter, the sign of N_{eff} becomes the only factor that determines the nature of the Hopf bifurcation for a beam with constant known parameters, Λ, Γ, and ω_n, hence, the sign of N_{eff} varies only with λ_{cr} which, in turn, depends on the critical gain K_{cr} and the critical delay γ_{cr} that are found via Equation (5-8) and Equation (5-9).

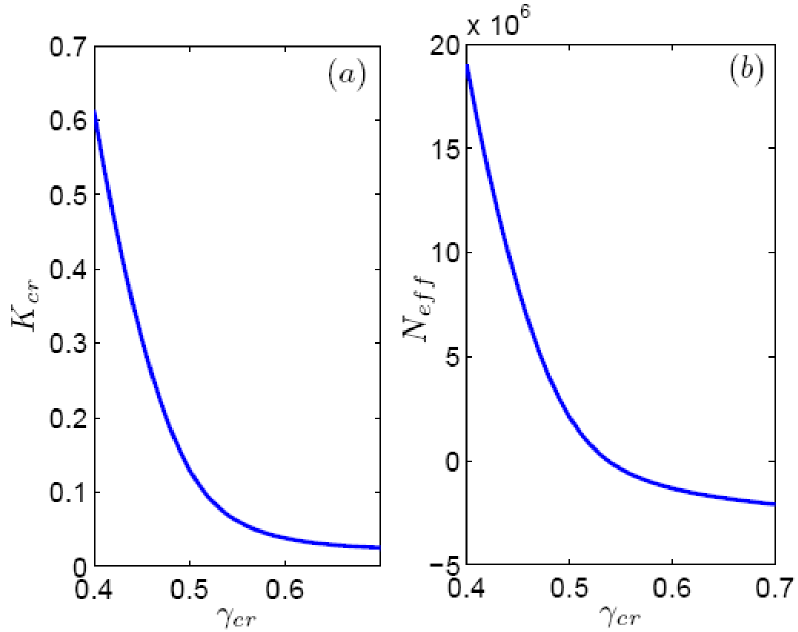

Figure 5.3 (a) Stability boundary of the trivial solutions of Equation (5-4), (b) Variation of the effective nonlinearity coefficient N_{eff} with the critical delay γ_{cr} along the stability boundary shown in (a). Results are obtained for nu = 0.025 [67]

Figure 5.3(b) illustrates variation of the effective nonlinearity with γ_{cr} along the stability boundary shown in Figure 5.3(a). For small γ_{cr}, the effective nonlinearity is large and positive, meaning the system is highly nonlinear. One would then correctly surmise that nonlinearities limit the growth of the response significantly. However, as γ_{cr} increases, N_{eff} decreases and approaches zero near γ= 0.54. At this point the system exhibits a linear behavior because there are no response-limiting nonlinearities. This causes solutions to grow without bound. Further increase of γ_{cr} results in negative values for N_{eff} .

To determine the nature of the Hopf bifurcation, we examine conditions in which K_2<0 and N_{eff}>0, we find that Equation (5-21) has only the stable trivial solution a = 0.

Alternatively, when K_2>0 and N_{eff} remain positive, Equation (5-21) has three fixed points. Further evaluation of their stability indicates that these points include an unstable trivial solution a = 0 and stable nonzero solutions:

$$a = \pm 2\sqrt{-\frac{K_2 \omega_n^2 H_1}{N_{eff} v}} \tag{5-26}$$

Since the bifurcating nontrivial (periodic) solutions are stable, the Hopf bifurcation is supercritical. Consequently, any initial disturbances will disappear for $K < K_{cr}$ and will result in a stable limit-cycle for $K > K_{cr}$.

In the case $K_2 > 0$ and $N_{eff} < 0$, Equation (5-21) has only an unstable trivial solution a = 0, on the other hand, when $K_2 < 0$ and $N_{eff} < 0$, the solution of Equation (5-21) yields the three fixed points,

$$a = 0 \tag{5-27}$$

$$a = \pm 2\sqrt{-\frac{K_2 \omega_n^2 H_1}{N_{eff} v}} \tag{5-28}$$

However, in this situation, the trivial solution is stable and the bifurcating periodic solutions are unstable resulting in a subcritical Hopf bifurcation. Hence, any initial disturbances will disappear for $K < K_{cr}$ and will grow without bound for $K > K_{cr}$.

Amplitude and stability of the resulting limit-cycles

The solution obtained using the method of multiple scales is only valid very close to the stability boundaries and deviates significantly from the actual solution as we shift away from these boundaries. In order to obtain accurate cantilever responses and assess their stability everywhere in the gain-delay domain, we analytically construct the limit cycles using the Method of Harmonic Balance and check their stability using the Floquet theory [64]. These results are illustrated in Figure 5.4 which displays variation of the limit cycle amplitude with the feedback gain K for different time-delays. By examining these variations, we can easily observe the effect of the nonlinearity on the amplitude of the limit cycles. For larger delays, there is a sharper increase in the oscillation amplitude as compared to smaller delay values. This stems from the fact that, as the delay increases, the effective nonlinearity N_{eff} decreases as depicted previously in Figure 5.4. As a result, the response becomes more linear causing the amplitude of the response to grow faster as we cross the stability boundaries of the trivial solutions. Furthermore, the percentage increase in the limit-cycle amplitude is large very close to the bifurcation point (i.e., smaller amplitudes) and tends to decrease when K is far from the critical gain K_{cr} (i.e., larger amplitudes). These two points clearly demonstrate that the limit-cycle amplitude is more sensitive to variation in K for larger delays and smaller amplitudes.

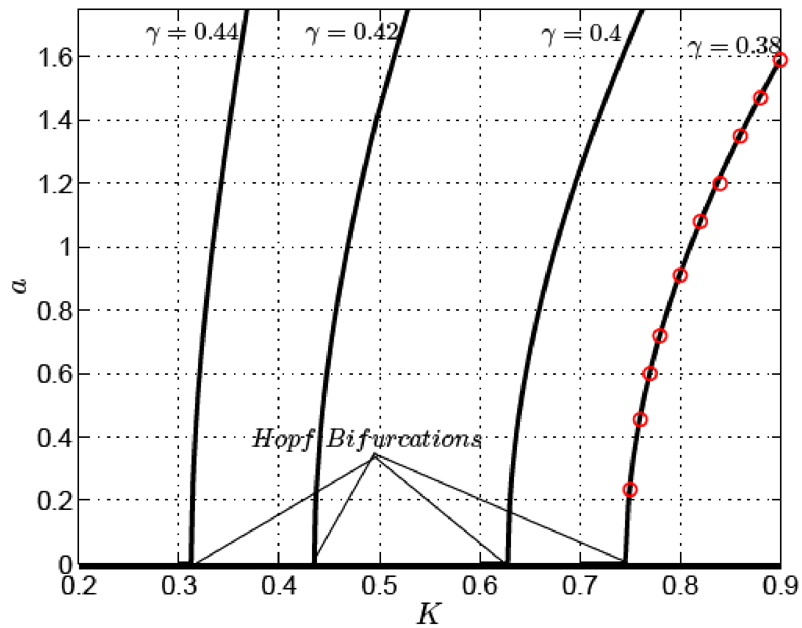

Figure 5.4 Variation of the limit-cycle amplitude with the gain K for different time-delays g. Solutions are obtained using the method of harmonic balance (solid lines) and compared to long-time numerical integration (circles) for γ = 0.38. [67]

Concept of Sensor Sensitivity Enhancement

In the preceding discussion, we described the effect of feedback delays on the linear and nonlinear response of cantilever beams. We have shown that the response undergoes a Hopf bifurcation (*supercritical for the most part*) leading to a stable limit cycle whose amplitude increases as we shift away from the stability boundaries. The concept of sensor sensitivity enhancement is based on utilizing these limit cycles to detect extremely small variations in the frequency. The technique is simple, does not require any changes or additions to the current sensor geometry or design, and most importantly can be implemented in real-time because it does not require any computational power. Moreover, the methodology allows us to incorporate any system delays into the parametric delay that is intentionally introduced for sensitivity enhancement. The principle works by choosing a gain-delay combination (K,γ) that is very close, but outside the stability boundaries illustrated in Figure 5.3. Intentional introduction of this delayed feedback to the excitation signal yields limit-cycle oscillations whose amplitude is equal to a. After this when an ultra small mass M is added to the beam tip, the amplitude of the resulting limit cycle changes significantly, even if the variation of the frequency ω_n is negligible. By relating the variation of the limit cycle amplitude to the added mass, one can detect the amount of added mass. Figure 5.5 illustrates the effect of increasing the tip mass from M = 0 mg to M = 30 mg on the percentage change of the response amplitude and natural frequency. It can be easily observed that, while the natural frequency variation is very small and is hardly detectable, the amplitude of the limit cycle varies significantly and can be easily detected even for extremely small masses.

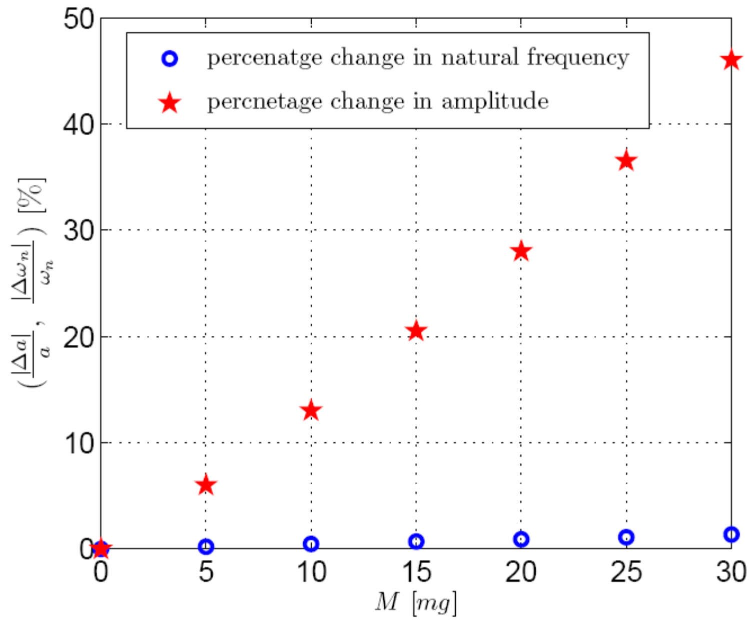

Figure 5.5 Percentage drop in the limit-cycle amplitude and natural frequency as function of the added mass. Results are obtained using the method of harmonic balance for a delay γ=0.4 and a gain *K*=0.615 [67].

One of the most desirable features of the proposed approach is the ability to vary the detection sensitivity by changing the gain-delay combination used. This allows for the detection of small as well as large frequency variations with equal precision and sensitivity. More specifically, using this approach, it is possible to make the limit-cycle amplitude very sensitive to frequency variations by choosing gains that are very close to the stability boundary and larger feedback delays, or make the response less sensitive, by choosing smaller feedback delays and larger gains. The importance of the preceding discussion is illustrated in Figure 5.6 where we show time histories of the cantilever response before and after adding three different masses to the beam tip. In this particular simulation, a very sensitive gain-delay combination is chosen to detect the addition of a 3 *mg* mass (less than 0.1% frequency variation). However, when the same gain-delay combination is used to detect larger masses (10 *mg*, 20 *mg*), the response amplitude drops to zero in both cases. This indicates the addition of two large masses but does not allow us to differentiate between them. Consequently, a less sensitive gain-delay combination is necessary to differentiate between these masses.

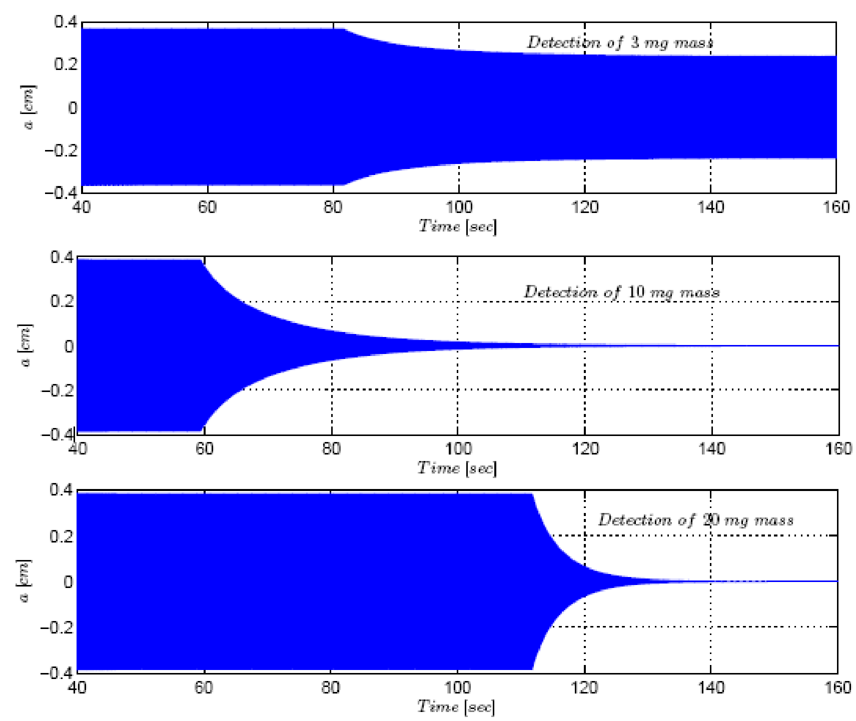

Figure 5.6 Time histories of the beam response before and after the addition of 3 masses to the beam. Results are obtained using long-time integration of the equations of motion [67].

Sensitivity Analysis

To assess the sensitivity to mass, it must be considered what manner of additional mass is going to be examined. To simplify the problem it is assumed that a uniform change in mass along the beam is encountered. This causes no change in beam geometry or mode shapes as would be the case for a tip mass or an added layer of mass on the surface of the beam. The effect of this additional mass is assumed to only affect the resonant frequency ω_n. Therefore, the goal is to first find the governing equation for amplitude, then find the derivative of this equation for changes in ω_n.

The sensor will be comprised of a fixed-free beam. We will consider this beam to be isotropic and inextensible as before. As before we find that the governing nonlinear equation of motion for the beam is as follows.

$$\ddot{v} + \mu\,\dot{v} + \omega_n^2 v = \Gamma v^3 + 2\Lambda \dot{v}^2 v + 2\,\Lambda \ddot{v} v^2 \qquad \textbf{(5-29)}$$

Over dots represent derivatives with respect to time. Γ and Λ represent inertial and geometric nonlinearities. Tip acceleration is then used as system feedback after a time-delay τ. This adds terms to the equation of motion as seen below,

$$\ddot{u} + \mu\,\dot{v} + \omega_n^2 v = -K\,\ddot{v}(t-\tau) + \Gamma v^3 + 2\Lambda \dot{v}^2 v + 2\,\Lambda \ddot{v} v^2 \qquad \textbf{(5-30)}$$

where α and β are positive constant properties of the beam.

<u>Sensativity Solution</u>

We begin by expanding the amplitude modulation equation (5-21)

$$\dot{a} = -\frac{\pi^2 a\,(4K_2\omega n^2\mu\cos(\omega\tau) - 8K_2\,\omega n^2\sin(\omega\tau)\,\omega - 4\mu a^2\Lambda\omega^2 + 3\mu a^2\Gamma}{4\mu^2\pi^2 + \tau^2\omega n^4} \qquad \textbf{(5-31)}$$

From the modulation equation we find that the solution to the steady-state fixed points result in

$$a = -2\frac{\sqrt{(\mu(3\Gamma - 4\Lambda\,\omega^2)K_2\,(\mu\cos(\omega\,\tau) + 2\sin(\omega\,\tau)\ \omega)}\,\omega_n}{\mu\,(3\Gamma - 4\Lambda\,\omega^2)} \quad \textbf{(5-32)}$$

The derivative of the amplitude with respect to ω_n can be obtained as

$$\frac{da}{d\omega} = -2\sqrt{K_2}\sqrt{(4\beta\omega^2 - 3\alpha)(\mu\cos(\omega\tau) + 2\sin(\omega\tau)\,\omega}\,\frac{\omega}{\sqrt{\mu}\,(3\Gamma - 4\Lambda\,\omega^2)} \quad \textbf{(5-33)}$$

From the linear system we obtain.

$$\lambda\left(2\,\zeta + \frac{\mu}{\omega_n}\right)\mathrm{e}^{2\,\pi\,\zeta\,\gamma} + K\sin(\omega\,\tau) = 0 \quad \textbf{(5-34)}$$

$$\left(\left(\frac{\omega}{\omega_n}\right)^2 - \zeta^2 - \left(\frac{\mu}{\omega_n}\right)\zeta - 1\right)e^{2\pi\zeta\gamma} + K\cos(\omega\,\tau) = 0 \quad \textbf{(5-35)}$$

However, we know that in order to be on or very near the stability boundary, $\zeta = 0$ must hold. Therefore, for critical values of K, ω and τ the equations become.

$$\frac{\omega}{\omega_n}\frac{\mu}{\omega_n} + K_{cr}\sin(\omega\,\tau) = 0 \quad \textbf{(5-36)}$$

$$\left(\left(\frac{\omega}{\omega_n}\right)^2 - 1\right) + K_{cr}\cos(\omega\,\tau) = 0 \quad \textbf{(5-37)}$$

Substituting these back into the sensitivity equation yields the sensitivity of the system to changes in frequency as:

$$\frac{da}{d\omega} = \frac{2}{\omega_n}\sqrt{\frac{K_2}{K_c}}\frac{\sqrt{(\omega n^2 + \omega^2)}}{\sqrt{4\Lambda\,\omega^2 - 3\Gamma}} \qquad \textbf{(5-38)}$$

This gives us the sensitivity for the system as we have defined it. We note that the sensitivity is a function of the critical gain K_c so by choosing τ_{cr}, the sensitivity can be selectively tuned. This expression can be further simplified with the assumption that $\omega_n \cong \omega$ resulting in.

$$\frac{da}{d\omega_n} = 2\sqrt{2}\sqrt{\frac{K_2}{K_c}}\frac{1}{\sqrt{4\Lambda\,\omega^2 - 3\Gamma}} \qquad \textbf{(5-39)}$$

This shows that the primary factors that affect the sensitivity of the method is the effective nonlinearity and the ratio of K_2 and K_c. The value for K_c can be tuned by varying the delay.

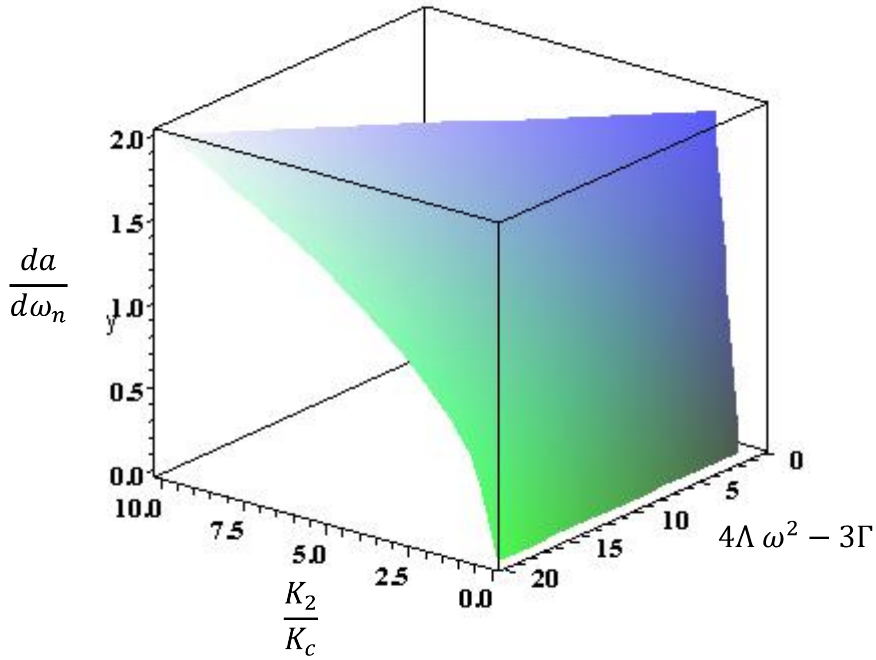

Figure 5.7 Sensitivity of oscillation amplitude to frequency shifts

As illustrated in Figure 5.7 we see that sensitivity increases as the ratio of K_2 to K_c increases as well as minimizing $4\Lambda\,\omega^2 - 3\Gamma$. Solutions can only occur if $4\Lambda\,\omega^2 - 3\Gamma$ is positive. This enables tunable sensitivity for higher sensitivity with the same value for K_2 changing delay to allow for a lower K_c would increase the sensitivity.

An expression for the sensitivity close to the stability boundary was derived and it was shown that the sensitivity is primarily a function of the inverse of the square root of the effective nonlinearities, and the square root of the ratio of critical gain to the different between the operating gain and the critical gain. By changing the delay and thereby changing the critical gain, the sensitivity of a single cantilever can be tuned without the need of making any physical changes to the beam.

Preliminary Results on Macro CSS

The proposed methodology was implemented on the piezoelectrically-actuated stainless-steel cantilever beam depicted in Figure 5.8. The beam has dimensions 0.52" x 5.2"x 0.01" and is excited using a Macro Fiber Composite MFC patch. The combined first-mode natural frequency of the beam and the PZT was experimentally obtained as $\omega_n \approx 14.9$ *Hz*. The feedback signal which represents the deflection of the beam tip was measured utilizing a KAMAN LTS-946 laser sensor.

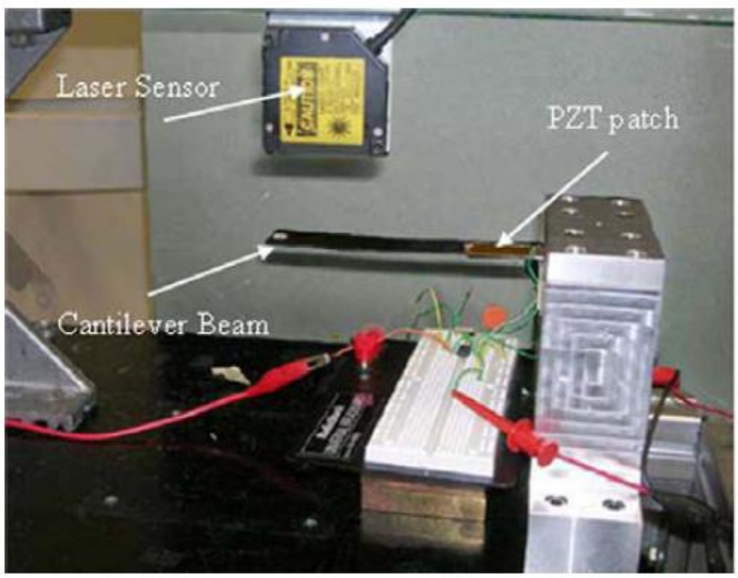

Figure 5.8 Piezoelectricaly-actuated macro CSS for testing delayed feedback in CSS.

In the first experiment, Figure 5.9, we verify the prediction of the linear theory by displaying a comparison between the stability boundaries obtained experimentally and that obtained theoretically for a range of feedback gains and time-delays. Results show excellent agreement, thereby, verifying the theoretical derivation of the proposed approach. To demonstrate the sensitivity enhancement attained by utilizing this algorithm, we conducted series of experiments in which we chose a specific feedback delay γ, and incrementally increased the feedback gain K until we observed measurable oscillations. The associated value of the gain represents the bifurcation point, $K = K_{cr}$. The gain K was then slightly increased beyond K_{cr} such that we attain a stable limit cycles oscillations of known amplitude a. A mass, M, was added to the tip of the beam and the experiments were repeated using the exact gain-delay combination. Limit cycles of much smaller amplitudes were observed. It is worth noting that, larger gains may excite higher vibrations modes and might cause the limit cycles to lose stability via a series of secondary Hopf bifurcations culminating in chaotic responses. Therefore, it is necessary that the gain chosen be very close to the critical value K_{cr}.

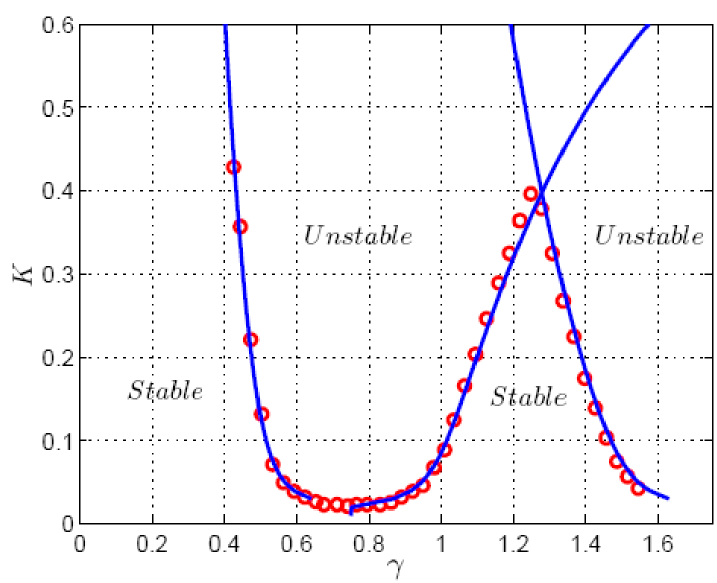

Figure 5.9 Comparison between the stability boundary obtained experimentally and that obtained via Equations (5-8) and (5-9) [67]

In Figure 5.10, we show one experiment in which the addition of 16.5 *mg* on the tip of the cantilever is detected using the proposed algorithm. The addition of this mass causes less than 0.6% shift in the first-mode natural frequency. Due to air damping and experimental errors (e.g., noise, temperature variations, etc.), this frequency variation is very hard to detect. However, as shown in Figure 5.10, using a gain K = 0.125 and a feedback delay γ = 0.5, a gain-delay combination which lies very close but outside the stability boundary illustrated in Figure 5.9, the addition of this tip mass causes about 58% drop in the limit-cycle amplitude. This constitutes two-orders-of-magnitude sensitivity enhancement over traditional frequency-shift methods.

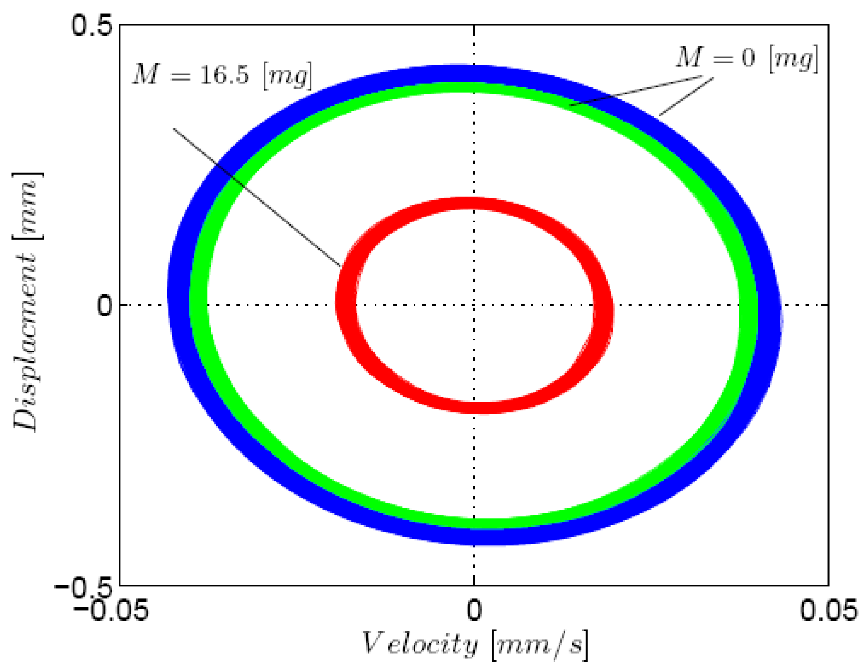

Figure 5.10 Variation of the limit-cycle amplitude due to the addition of 16.5 mg tip mass to a cantilever beam subjected to delayed-position feedback with gain K = 0.125 and delay γ = 0.5. The outer limit cycles are obtained before adding and after removing the tip mass.

Further Testing

A second experiment is conducted on an enclosed *Newport RSi* 1000 optical table. The beam under consideration has dimensions of 0.52 *in x* 3.38 *in x* 0.01 *in*, a modulus of elasticity E=200GPa, and a density ρ = 7800kg/m^3. The beam is subjected to base excitations from *CSA Engineering's SA*-5 inertial actuator. The tip displacement is again measured via a *KAMAN LTS*-946 laser displacement sensor at a location approximately 0.2 *in* from the beam tip. The tip-displacement measurement signal is run through a *dSPACE* data acquisition (DS1104) controller board, delayed in time, and then amplified using an *AVL* 790 series power amplifier before it is fed back to the inertial actuator. Masses, which comprise of small amounts of metal, are added to the small area between the laser and the end of the beam. The schematic of the experiment is shown in Figure 5.12. Following the common practice, we used a bandpass filter to remove low- and high-frequency excitations, thus preventing the resonant excitation of the inertial actuator and mitigating generic high-frequency noise as well as higher-mode oscillations. The second-order Butterworth bandpass filter utilized introduced a time-delay of 6/1000 seconds. For the purpose of sensitivity enhancement, additional time-delay period is deliberately introduced via the variable transport delay function in SIMULINK.

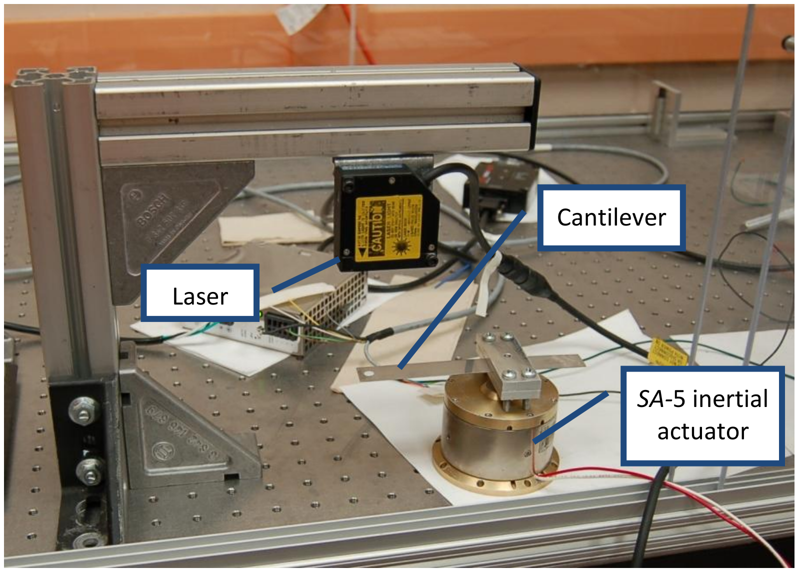

Figure 5.11 Base-excited macro CSS for testing delayed feedback in CSS.

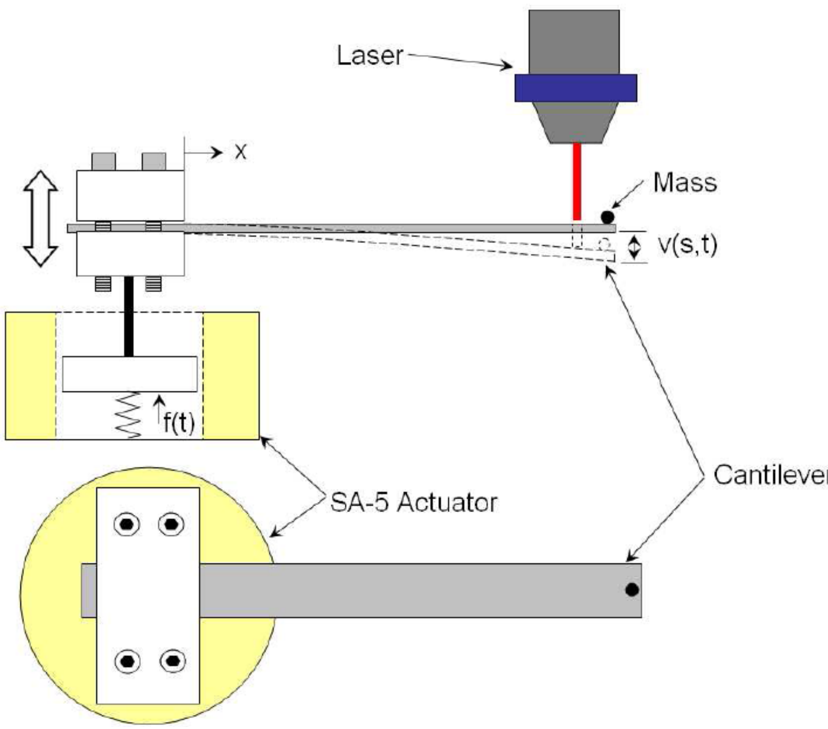

Figure 5.12 Schematic of a cantilever beam subjected to delayed-position feedback base excitations.

For the beam under consideration, we measured the first mode natural frequency at 45 *Hz* and the damping ratio at 0.0053. In the first set of experiments (see Figure 5.9), we verified the prediction of the linear theory by displaying a comparison between the stability boundary obtained experimentally and that obtained theoretically. The values for the Hopf bifurcation points at a given gain-delay combination are again experimentally obtained on the new setup via two different procedures. The first is conducted by starting with a gain-delay combination outside the stability boundaries then gradually decreasing the gain until the beam oscillations dropped to zero. While, in the second approach, the gain-delay combination is chosen initially in the linearly-stable region then the gain is increased until the onset of oscillations. In both cases, the theoretical and experimental results are in good agreement; however, results did not agree as well as previous experiments due to much higher stiction in the inertial actuator. Despite this, the repeatability was improved due to PZT elements dependence on temperature.

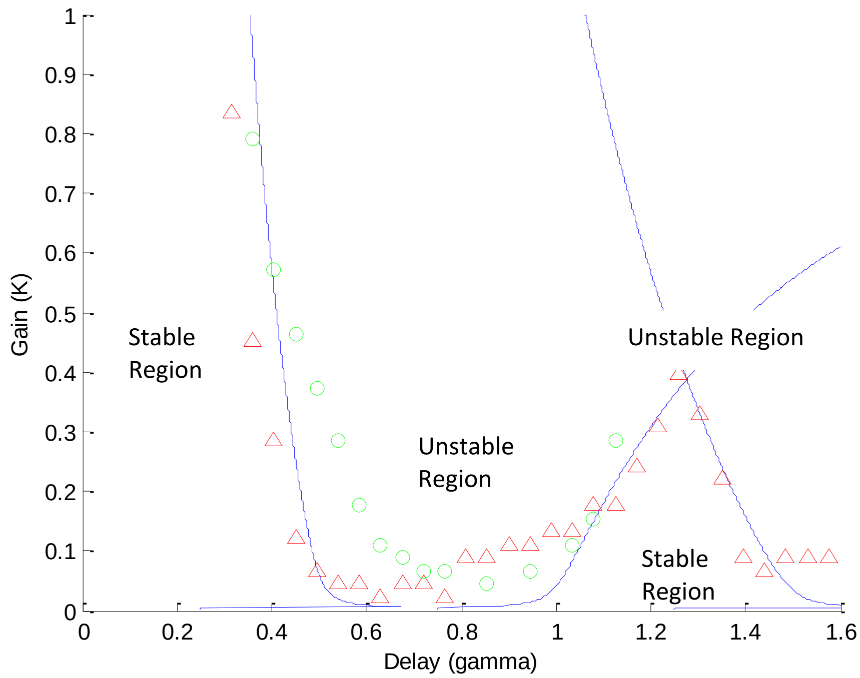

Figure 5.13 Stability pockets of Equation (5-4). Stable regions represent gain-delay combinations leading to asymptotically stable cantilever response. Solids lines represent theoretical stability boundaries; triangles (sweep up) and circles (sweep down) represent the onset of the Hopf bifurcation points. This chart is obtained for n = 0.0053 [71].

To examine the nature and stability of the resulting limit cycle oscillation, we study variation of the response amplitude with the gain K for a given time-delay, $\gamma = 0.35$. The results are displayed in Figure 5.14. As the gain is increased, the trivial solutions remain stable (i.e., no beam oscillations are measured) as long as the gain is below a critical value $K_{cr} \approx 0.35$. At that point, a supercritical Hopf bifurcation occurs and stable limit-cycle oscillations are born. As the gain is increased further, the amplitude of the resulting limit cycle increases sharply initially, and gradually as the gain is increased even further.

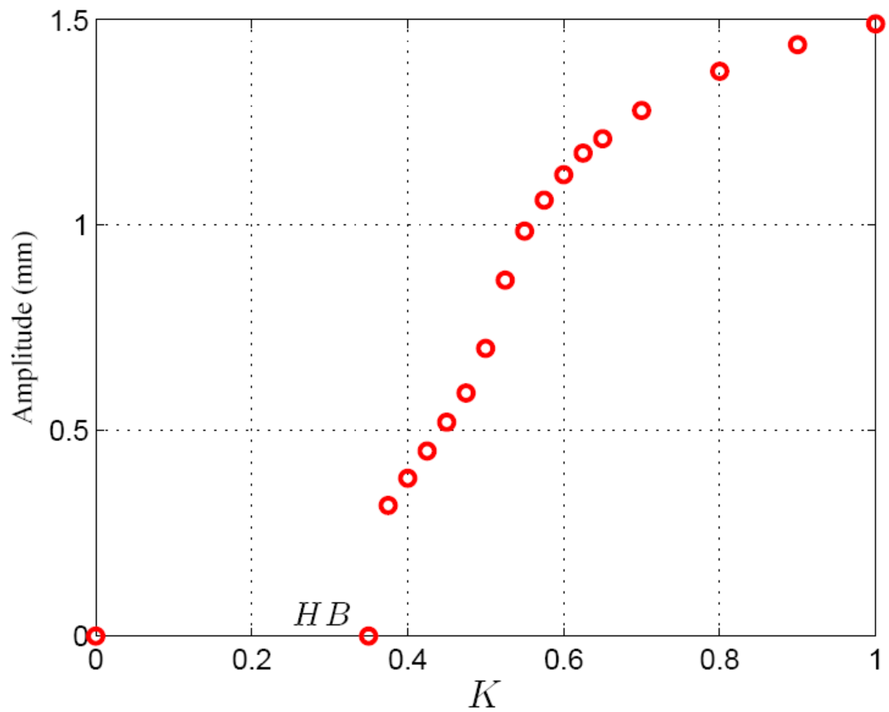

Figure 5.14 Variation of the limit cycle amplitude with the gain K for time-delay γ=0.35. The results are obtained experimentally for the cantilever beam under consideration [71].

To illustrate the effect of the time-delay on the limit cycles, we also display variation of the response amplitude as a function of the gain for different time-delays. Figure 5.15 illustrates that, for a given gain sweep, there is a sharper increase in the response amplitude for larger delays. Consequently, the limit-cycles are less sensitive to gain variations for small delays and more sensitive for larger values.

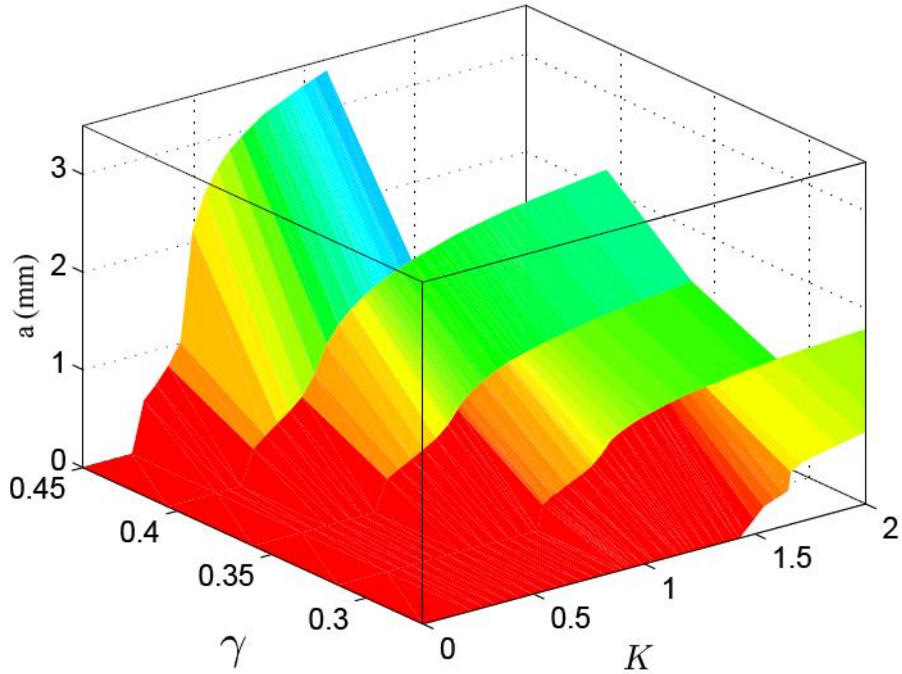

Figure 5.15 Variation of the limit cycle amplitude with the gain K and the delay γ. The results are obtained experimentally for the cantilever beam under consideration [71].

This constitutes a major advantage because it enables variations in the sensor sensitivity as previously shown. The availability of a vast number of gain-delay combinations that produce stable limit cycles allows for the design of a tunable sensor that can detect small as well as large frequency variations with equal precision and sensitivity. More specifically, using this concept, it is possible to choose limit-cycles that are very sensitive to frequency variations. This can be realized by choosing gains that are very close to the stability boundary and large feedback delays. On the other hand, one can also make the response less sensitive, by choosing smaller feedback delays and larger gains. More importantly, this tuning is achieved without changes to the equipment or the sensor geometry.

Sensitivity enhancement is accomplished by taking advantage of the sharp variation of the limit-cycle amplitude close to the bifurcation point. Towards that end, the gain and delay are chosen such that the beam response is at a desired location on the bifurcation diagram, usually slightly beyond the Hopf bifurcation point. Therefore, small variations in the system parameters yield significant amplitude variations. As an initial test, we chose a gain-delay set consisting of $K = 0.44$ and $\gamma = 0.45$. Without added mass, we measured the limit-cycle amplitude at 0.75 *mm*. afterwards, different masses were attached to the tip of the beam and the limit-cycle amplitudes were recorded. It was observed that the amplitude of the limit cycle decreases as the mass is increased. For large masses, the amplitude drops back to zero where the system is no longer sensitive to parameter variations. This, however, does not constitute a disadvantage of the proposed methodology, since the technique is aimed at detecting ultra-small masses. The results were also repeated for the same and different gain-delay combinations. The addition of different mass usually resulted in consistent and repeatable limit cycle amplitude variations. These results are displayed in Figure 5.16, showing well-defined limit cycles and significant variations in the response-amplitude.

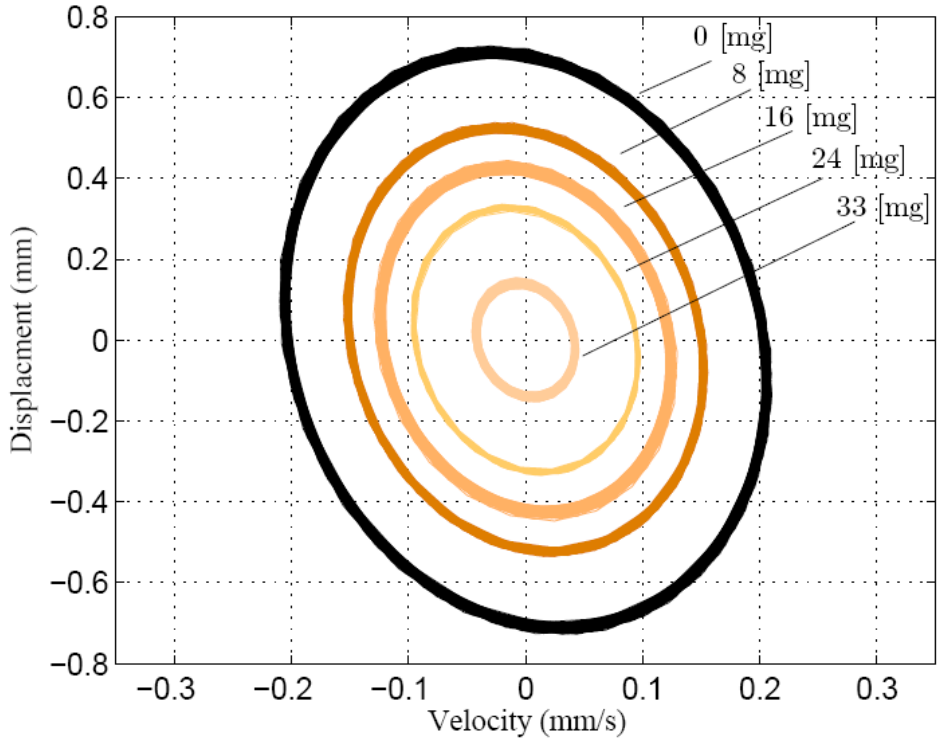

Figure 5.16 Variation of the limit-cycle amplitude due to the addition of various tip masses to a cantilever beam subjected to delayed-position feedback with gain K=0.44 and delay γ=0.45 [71].

The sensitivity of the proposed methodology is compared to the traditional frequency-shift method in Figure 5.17. The variation of the resonant frequency for various masses is determined by utilizing a 16384 point Fast Fourier Transform (FFT) of the free response of the beam to an initial condition. Because of the nonlinearity, the oscillation frequency has a weak dependence on the initial amplitude, therefore the frequency measurements were averaged over four iterations. The results are compared with the sensitivity-enhancement approach utilizing a feedback delay, γ=0.45 and a gain *K*=0.44. Results clearly show orders of magnitude sensitivity enhancement over the traditional frequency-shift method and show excellent agreement with Figure 5.5.

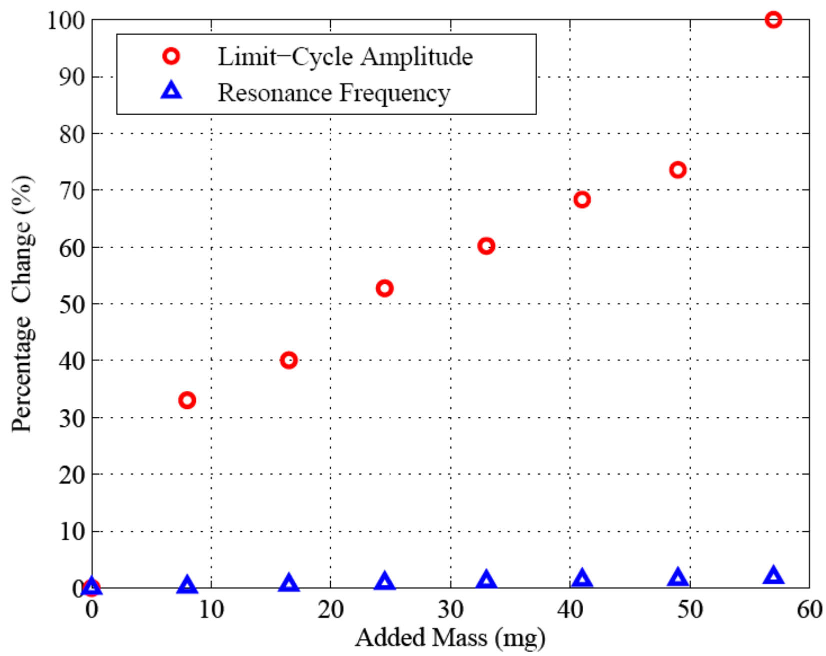

Figure 5.17 Percentage drop in the limit-cycle amplitude and resonance frequency as function of the added mass. Results are obtained experimentally for a delay γ = 0.45 and a gain *K* = 0.44 [71].

Summary

In this chapter, we presented a simple yet, effective technique for CSS sensitivity enhancement using delayed-position feedback. The technique utilizes system nonlinearities to create stable limit-cycle oscillations whose amplitude is ultra-sensitive to frequency variations. The proposed approach was implemented on a cantilever beam and used to detect the addition of very small tip masses. Experimental results demonstrated two-orders-of magnitude sensitivity enhancement over traditional frequency shift methods. Currently, we are in the process of verifying the predictions of the nonlinear theory by comparing the limit-cycle amplitude obtained experimentally to that obtained using the proposed model. Once this approach is verified, we will analytically construct the response amplitude in terms of the frequency variation and use the resulting expression to calculate the frequency shift. Afterwards, the technique will be implemented on micro CSS.

CHAPTER 6 : CONCLUSIONS AND FUTURE WORK

Summary

This thesis gave an overview of CSS beginning with the history and then continuing to the state of the art. The working principles of CSS were covered to provide a background for topics. An introduction of the two basic modes of operation was then given. Following this, transduction methods and fabrication techniques were introduced. This served as a basis for the remaining chapters that covered experimentation and advances in CSS.

Chapter 3 dealt with a novel and new application for the first operational mode of CSS. In order to understand this new application, PNIPAM thermally sensitive polymers are briefly introduces and overviewed. Then, the experimental setup illustrated the usefulness of a multi-cantilever array using reference beams to isolate functional effects. Results demonstrate the usefulness of CSS in this new application. The test also showed some of the difficulties with current techniques.

Chapter 4 covered the fabrication and testing of a new cantilever design with a transduction method utilizing an integrated strain gauge. This advancement resolves some of the issues with optical transduction methods by decreasing the size and cost of apparatus while still correcting for environmental effects. These new cantilevers were tested using the second operational mode for CSS to detect the presents of Au nanoparticles.

Chapter 5 dealt with advancing the primary function of CSS, i.e., their sensitivity. This was accomplished utilizing a time-delayed position feedback. Effects of time-delay were discussed by looking at first the linear then nonlinear problem. This resulted in a limit cycle that has amplitude much more sensitive to additional mass when compared with traditional methods of utilizing changes in frequency. The problem was solved utilizing the method of multiple scales, followed by the tunability of the sensitivity. The method was then demonstrated utilizing two different macro CSS and stability results were compared with the developed theory. Results for the new method were also compared to the traditional method.

Conclusions

Cantilever Sensing Systems (CSS) have become a focal area for research with the rise of micro- and nanotechnology. The history shows the evolution of the cantilever becoming one of the foremost sensing devices for small scale applications, beginning with the atomic force microscopy, and then being expanded into numerous sensor devices. CSS are expanding into applications of mass and material property sensing.

This study covered the experimentation into the new applications and sensitivity enhancements. In order to do this and overview of CSS was presented. The history of cantilever was covered from its humble beginnings to the recent explosion of interest following the development of the AFM. Working principles, operational modes and microfabrication are overviewed.

Experimentation into a novel CSS application of property change measurement of a thermally sensitive polymer was shown. The results show that static mode CSS using optical transduction can be effectively used to sense a polymer's lower critical solution temperature via measuring the surface stress caused by the said polymer. However, the process required expensive tedious and bulky apparatus.

A new dynamic mode CSS design was fabricated and used in mass detection. This new design measured the relative frequency shift of the functional CSS with respect to a reference CSS in order to provide environmental effect compensation. This was observed utilizing integrated strain gauges that have the potential to make sensors smaller, more inexpensive, and less tedious than optical methods. These CSS were demonstrated effective by sensing the frequency shift due to addition of Au nanoparticles.

Finally, an exciting new technique to enhance CSS sensitivity was developed and demonstrated. The new technique utilized a delayed feedback to create stable limit cycles. The amplitude of these limit cycles shows highly sensitive to changes in mass of the cantilever. The theory was presented and verified utilizing macroscale experimentation demonstrating a two-orders-of magnitude sensitivity enhancement over traditional frequency shift methods.

Future Work

Research into delayed feedback sensitivity enhancement is underway at Clemson's Smart Structures and Nanomechanical Systems laboratory. This work is being done to bring this new method to the microscale where it can become an effective new tool in the quest for creating ideal CSS. These new systems could then utilize transduction techniques such as an integrated strain gauge. Characterization utilizing deposition of Au nanoparticles could verify sensitivity. Or the use of an integrated and encapsulated Au strain gauge could be utilized as a small and inexpensive device to detect polymer, or other material, properties as a function of temperature with integrated environmental correction.

In addition to this, current work is being done utilizing a piezoelectrically actuated AFM cantilever with various masses added in differing locations utilizing a focused ion beam (FIB) to make the depositions as well as removal of material as shown in Figure 6.1.

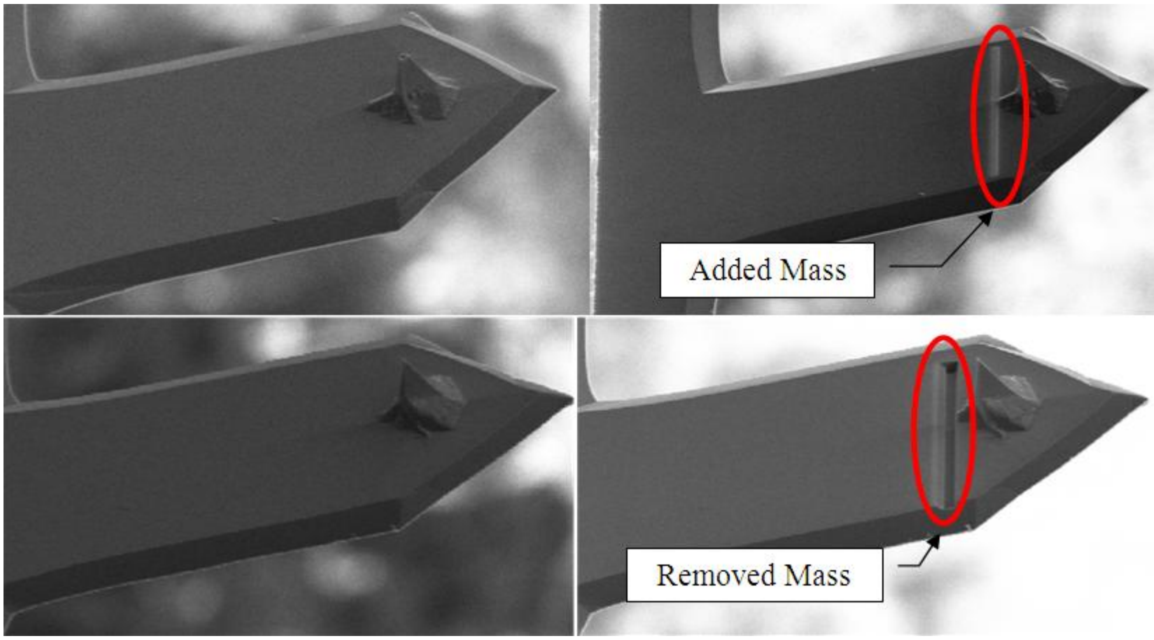

Figure 6.1 SEM image of piezoelectrically actuated AFM cantilevers before and after mass has been added and removed utilizing a FIB technique.

Utilizing the nonlinear dynamics, it is desired to use the resulting mode shapes to be able to determine not only the amount of additional mass but also location as well, creating even more avenues of use for CSS [72]. This would also prove useful when determining the actual amount of mass that has been added to a CSS, because it would enable compensation for mass that was added at location other than tip. This would, in addition, enable the use of the entire cantilever as the functional surface area.

APPENDIX

Additional Figures

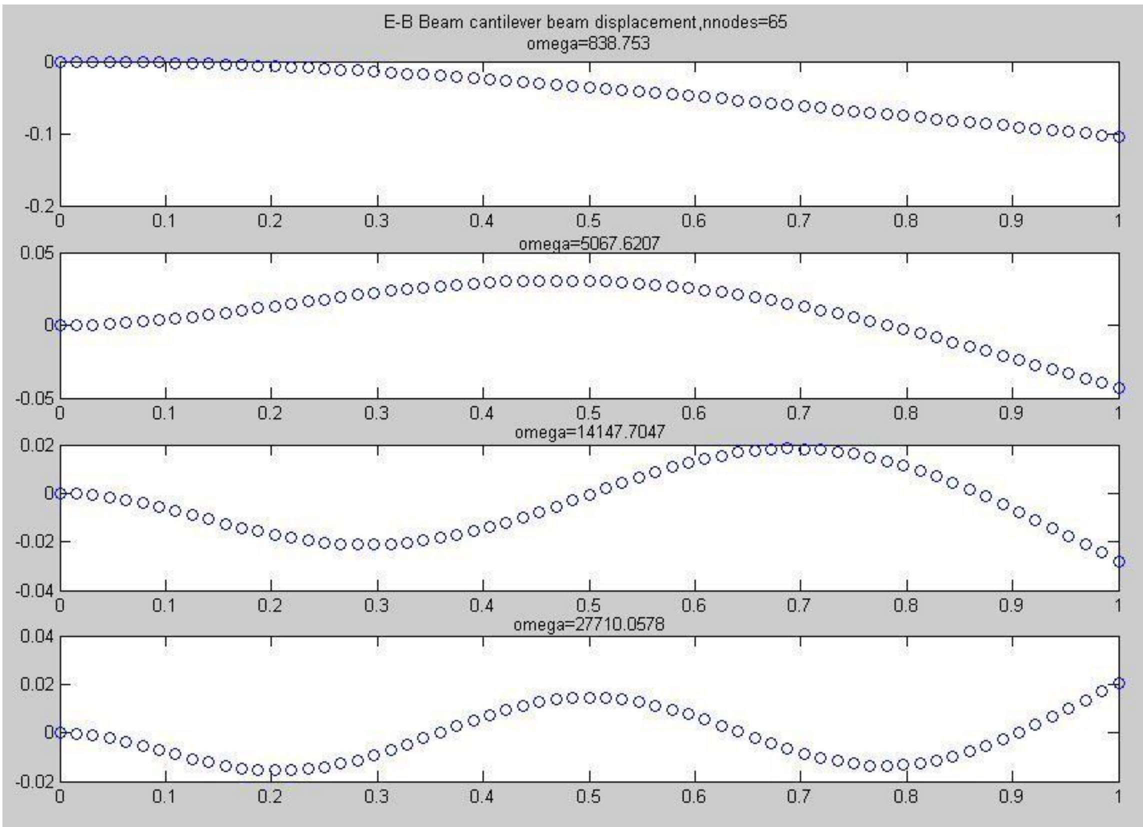

Figure A.1 FEA simulated mode shapes verifying derived mode shapes

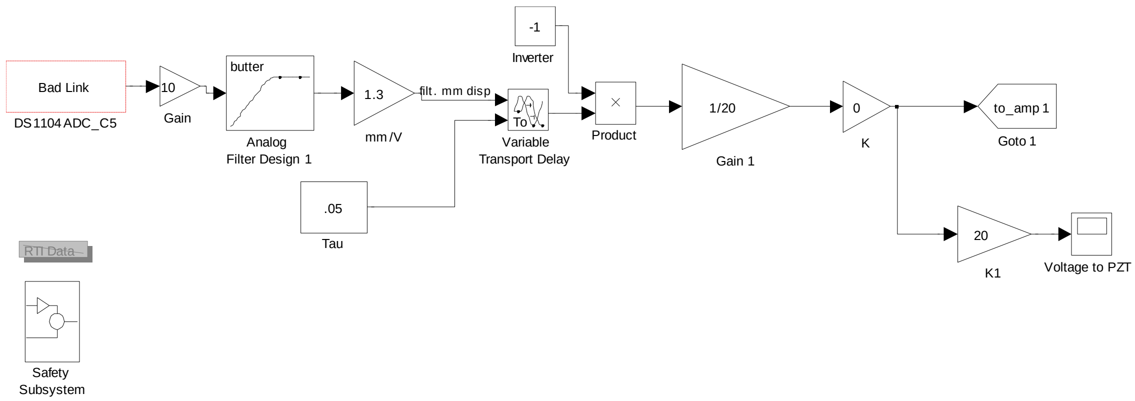

Figure A. 2 SIMULINK model for delayed feedback with D-Space DS1104 interface

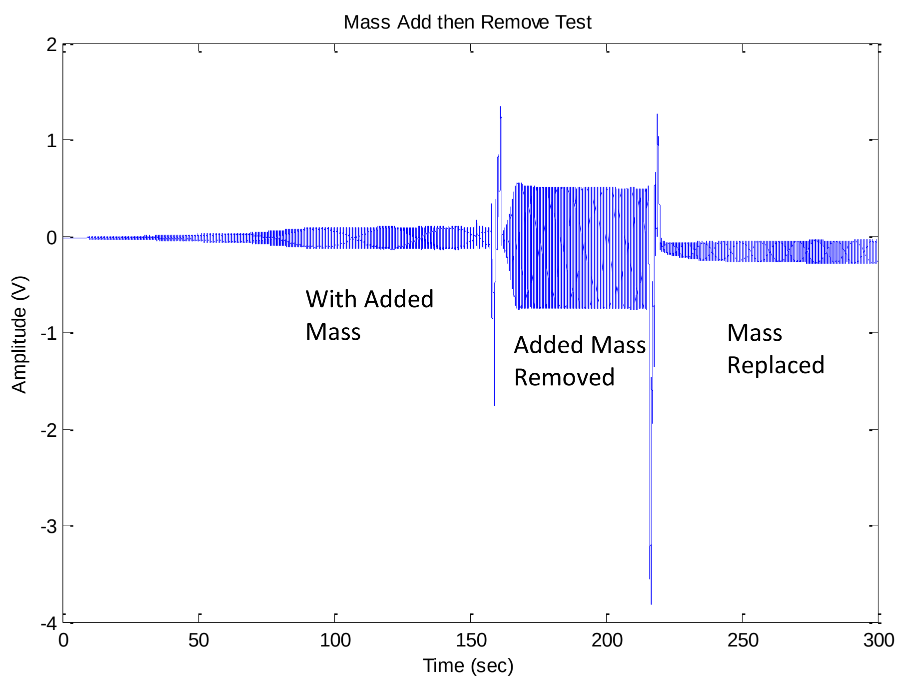

Figure A. 3 Time history of delayed feedback test showing first the response with Mass

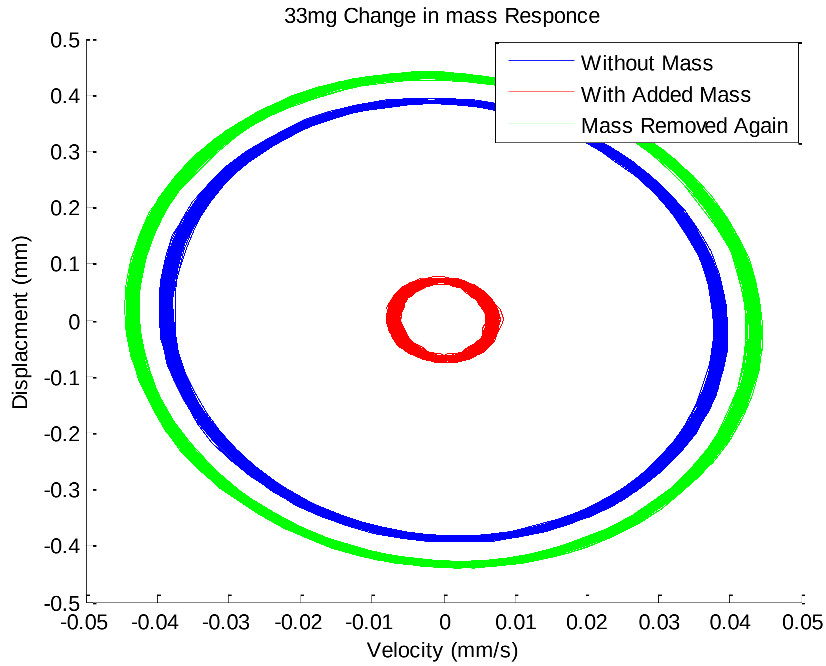

Figure A. 4 Piezoelectrically-actuated cantilever delayed feedback induced limit-cycle magnitude mass sensitivity.

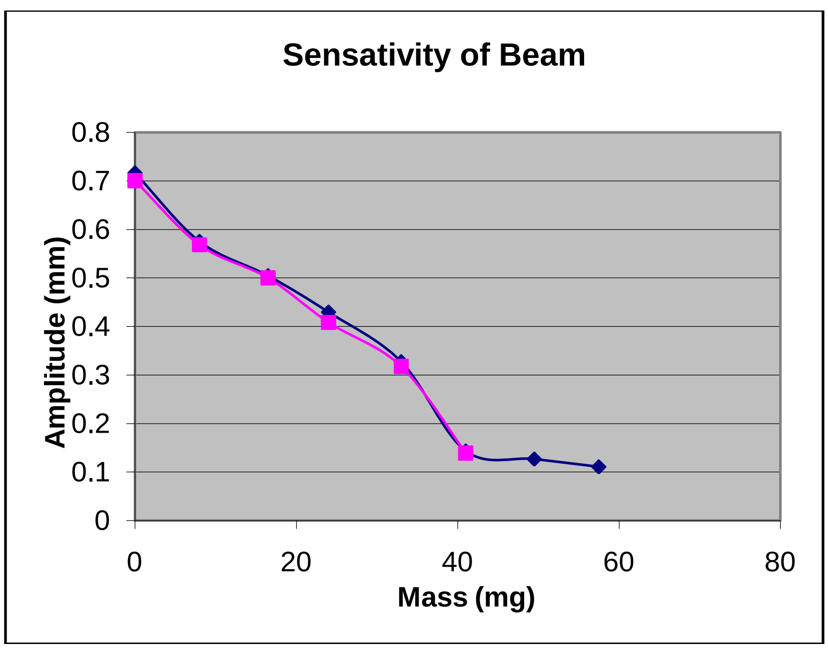

Figure A. 5 Amplitude sensitivity of delayed feedback enhanced base excitation CSS demonstrating excellent repeatability.

Sample Matlab Code

The following is Matlab code for analysis of PNIPAM functionalized CSS.

```
clc
clear all
xlimit=[26 39]


%Polymer Brush 1 049
%*************************************************
%  Place Data location here
t_T=importdata('polymer brush 049\pbrush_temp_000.txt');          % Temp vs Time
data
Y_t=importdata('polymer brush 049\pbrush_dis_000.txt');                  % Y is
displacment
%  Experiment Details
test='Polymer Brush chip 049 Test 002';
%   Beam Data Assignment
funcbeams=[1 2 3 4];       %    functional beams plus 1
refbeams=[6 7 8];          %    Reference beams plus 1
leg=['F 1';'F 2';'F 3';'R 4';'R 5';'R 6']
%  Axis Titles
diffaxis='Average Difference in Stress (kPa)';
avgaxis='Averaged Deflection (kPa)';
absaxis='Absolute Deflection (kPa)';
tempaxis='Temperature (C)';
% Data Calculations
funcbeams=(funcbeams+1)*2-2;
refbeams=(refbeams+1)*2-2;
timeY=Y_t(:,1);
fbY=Y_t(:,funcbeams);
rbY=Y_t(:,refbeams);
% Convert deflection to surface stress with Stoneys equation
% Stoneys Values
%*******************************************
tc=7E-9                     % coating thickness
d_2_st=(112.4E9*(1E-6)^2)/(15*tc*(450E-6)^2);  % Stoneys Equation for displacement
 fbY=fbY*1E-12.*d_2_st;
 rbY=rbY*1E-12.*d_2_st;
%  Get Common Time and Tempurature
```

```
T=t_T(:,2);              % Temp curve
Ti = interp1(T,timeY);  % temperature at time
fbA=mean(fbY');
rbA=mean(rbY');
diff=fbA-rbA;
%*****************************************************
 % Plot difference with respect to temperature
figure(1)
subplot(2,2,1)
plot(Ti,diff,'b.')
xlabel('Temperature (C)')
ylabel(diffaxis)
title('Polymer Brush 049')
xlim(xlimit)
```

The following is Matlab code for plotting stability boundaries shown in Figure 5.13.

```
%clear all;
%Must SBound workspace
lambda1=4.8;
gamma1=6.9;
for g=[-1,1]
  for n=1:3
%       n=1;       % change n for different branches of the solution.
%       g=1;       % change the sign of g for different branches of the solution.
    %lambda=sqrt(3*gamma1/4/lambda1);
    omega_0=45*2*pi;
    mu=.0053*omega_0;
    nu=mu/omega_0;
    for i=1:1000;
      r=(i)/1000;
      K(i)=(i)/1000;
      lambda= sqrt(2-nu^2+ g *sqrt(4*K(i)^2-4*nu^2+nu^4))/sqrt(2); %
      gamma(i)=1/(2*pi*lambda)*(atan(nu*lambda/(lambda^2-1))+n*pi);
      lamda3(i)=lambda;
    end
    figure(1)
    hold on;
```

```
      plot(gamma(:),K(:))
   end
end
axis([0 1.6 0 1])

%*********************************************************************
****
Tau=SBound(:,1);
K=SBound(:,2);
gama=(Tau+.006)./(1/45);
K1=(K-.62)*2.2;
plot(gama,K1,'^r')
xlabel('Delay (gamma)')
ylabel('Gain (K)')

% settling bifurcation point
% Load SB data
plot((Tau_K(:,1)+.006)./(1/45),...
   ((Tau_K(:,2)-.0)*2.2),'og');
legend('Decreasing Gain','Increasing Gain')
```

WORKS CITED

1. **Frank E. Jones, Randall M. Schoonover.** *Handbook of Mass Measurement.* s.l. : CRC Press, 2002. ISBN 0849325315.

2. **Rodahl, M., Hook, F., Krozer, A., Brzezinski, P. and Kazemo B.** "Quartz-crystal microbalance setup for frequency and q-factor measurements in gaseous and liquid enviroments.". *Review of Scientific Instruments.* 1995. Vol. 66, 7, pp. 3924-3920.

3. **Ekinci, K.L., Huang, X.M.H. and Roukes, M.L.** "Ultrasenssitive nanoelectromechanical mass detection". *Applied Physics Letters.* s.l. : Applied Physics Letters, 2004. Vol. 84, 22, pp. 4469-4471.

4. **Yang, Y.T., Callergari, C., Feng, X.L., Ekinci, K.L., Roukes, M.L.** "Zeptogram-scale nanomechanical mass sensing". *Nano Letters.* 2006. Vol. 6, 4, pp. 583-586.

5. **I., Oden P.** "Gravimetric Sensing of Metallic Deposits Using an End-Loaded Microfabricated Beam Structure". *Sensors and Actuators B.* 1998. 53, pp. 191-196.

6. **Godin, M., Tabard-Cossa, V., Grutter P. and Williams, P.** "Quantitative Surface Stress Measurements Using a Micro-Cantilever". s.l. : Appl. Phys. Lett., 2001. Vol. 79, 551.

7. **Taylor E.H. and Waggener, W.C.** "Measurement of Adsorptive Forces". *Journal of Physical Chemistry.* 1979. Vol. 83, 10, pp. 1361-1362.

8. **Jalili, N. and Laxminarayana, K.** "A Review of Atomic Force Microscopy Imaging Systems: Application to Molecular Metrology and Biological Sciences". *International Journal of Mechatronics.* 2004. Vol. 14, 8, pp. 907-945.

9. **Molhave, Kristian.** AFM Setup. *Wikicommons.* [Online] [Cited: March 08, 2008.] http://commons.wikimedia.org/wiki/Image:AFMsetup.jpg.

10. **Thundat T., Warmack R. J., Chen G.Y. Allison D.P.** "Thermal and Ambient-induced Deflections of Scanning Force Microscope Cantilevers". *Applied Physics Letters.* 1995. Vol. 66, 13, pp. 1695-1697.

11. **Gimzerwski J.K., Gerber Ch., Meyer E. and Schlittler R. R.** "Oberservation of a Chemical Reaction Useing a Micromechanical Sensor". *Chemical Physics Letters.* 1994. 217, pp. 589-594.

12. **Barnes J.R., Stephenson R.J., Woodburn C.N., O'Shea S.J., Welland M.E. and Gimzewski J.K.** "A Femtojoule Calorimeter Useing Micromechanical Sensors". *Review of Scientific Instruments.* 1994. Vol. 65, 12, pp. 3794-3798.

13. **Barnes J.R., Stephenson R.J., Welland M.E., Gerber Ch. and Gimzewski J.K.** "Photothermal Spectroscopy with Femtojoule Sensitivity useing a Micromechanical Device". *Nature.* 1994. 372, pp. 79-81.

14. **Lang H.P., Berger R., Battiston F., Ramseyer J.-P., Meyer E., Andreoli C., Brugger J., Vettiger P., Despont M., Mezzacasa T., Scandella L., Güntherodt H.-J., Gerber Ch. and Gimzewski J.K.** "A Chemical Sensor Based on a Micromechanical Cantilever Array for the Identification of Gases and Vapors". *Applied Physics A.* 1998. Vol. 66, 7, pp. s61-s64.

15. **H.-J., Raiteri R. and Butt.** "Measuring Electrochemically Induced Surface Stress with an Atomic Force Microscope". *Journal of Physical Chemistry.* 1995. Vol. 99, pp. 15728-15732.

16. **Thundat T., Chen G.Y., Warmack R.J., Allison D.P. and Wachter E.A.** "Vapor Detection Using Resonating Microcantilevers". *Analytical Chemistry.* 1995. Vol. 67, pp. 519-521.

17. **Thundat T., Wachter E.A., Sharp S.L. and Warmack R.J.** "Detection of Mercury Vapor Using Resonating Microcantilevers". *Applied Physics Letters.* 1995. Vol. 66, 13, pp. 1695-1797.

18. **T., Wachter E.A. and Thundat.** "Micromechanical Sensors for Chemical and Physical Measurements". *Review of Scientific Instruments.* 1995. Vol. 66, 6, pp. 3662-3667.

19. **Berger R., Gerber Ch. and Gimzewski J.K.** "Thermal Analysis Using a Micromechanical Calorimeter". *Applied Physics Letters.* 1996. Vol. 69, 1, pp. 40-42.

20. **Chen G.Y., Thundat T., Wachter E.A., and Warmack R.J.** "Adsporption Induced Surface Stress and Its Effects on Resonance Frequency of Microcantilevers". *Journal of Applied Phyiscs.* 1995. Vol. 77, 8, pp. 3618-3622.

21. **Datskos P.G., Oden P.I., Thundat T., Wachter E.A., Warmack R.J. and Hunter S.R.** "Remote Infrared Radiation Detection Using Piezoresistive". *Applied Physics Letters.* 1996. Vol. 69, 20, pp. 2986-2988.

22. **Oden P.I., Datskos P.G., Thundat T., and Warmack R.J.** "Uncooled Thermal Imaging Using a Piezoresistive Microcantilever". *Applied Physics Letters.* 1996. Vol. 69, 21, pp. 3277-3279.

23. **Perazzo T., Mao M., Kwon O., Majumdar A., Varesi J.B. and Norton P.** "Infrared Vision Using Uncooled Micro-optomechanical Camera". *Applied Phyisics Letters.* 1999. Vol. 74, 23, pp. 3567-3569.

24. **Ilic, B., Yang, Y. and Craighead, H.** "Virus Detection Useing Nanoelectricomechanical Devices". *Applied Physics Letters.* 2004. Vol. 85, 13, p. 2604.

25. **Zhang, J. and Feng, H.** "Antibody-immobilized Microcantilever for the Detection of Escherichia Coli". *Analytical Sciences.* 2004. Vol. 20, p. 585.

26. **Savran, C., Burg, T., Fritz, J. and Manalis, S.** "Microfabricated Mechanical Biosensor with Inherently Differential Readout". *Applied Physics Letters.* 2003. Vol. 83, 20, p. 1659.

27. **Hansen, K., Ji, H., Wu, G., Datar, R., Cote, R., Majumdar, A., and Thundat, T.** "Cantilever-based Optical Deflection Assay for Discrimination of DNA Single Nucleotide Mismatches". *Analytical Chemistry.* 2001. Vol. 73, 7, pp. 1567-1571.

28. **Pei, J., Tian, F., and Thundat, T.** "Glucose Biosensor Based on the Microcantilever". *Analytical Chemistry.* 2004. Vol. 76, p. 3194.

29. **Arntz, Y., Seelig, J., Lang, H., Zhang, J., Hunzicker, P., Ramseyer, J., Meyer, E., Hegener, M. and Gerber, C.** "Label-free Protein Assay Based on a Nanomechanical Cantilever Array". *Nanotechnology.* 2003. Vol. 14, 1, p. 86.

30. **Lee, J., Hwang, K. and Park, J.** "Immunoassay of Prostate-specific Antigen (PSA) Useing Resonant Frequency Shift of Piezoelectric Nanomechanical Microcantilever". *Biosensors and Bioelectronics.* 2005. Vol. 20, p. 2157.

31. **Dareing, D. and Thundat, T.** "Simulation of Adsorption-induced Stress of a Microcantilver Sensor". *Journal of Applied Physics.* 2005. Vol. 97, 4, pp. 043526–1–043526–5.

32. **Yang, Y., Ji, H. and Thundat, T.** "Nerve Agents Detection Useing a Cu/Lcysteine Bilayercoated Microcantilever". *Journal of American Chemical Society.* 2003. Vol. 125, 20, pp. 1124-1125.

33. **R., Koch R. and Abermann.** "On the Influence of Thermal Effects on Internal Stress Measurements during and After Deposition of Silver, Gold and Copper Films". *Thin Solid Films.* 1985. Vol. 129, pp. 63-70.

34. **Klein, Claude A.** "How accurate are Stoney's equation and recent modifications.". *Journal of Applied Physics.* 2000. Vol. 88, pp. 5487-5489.

35. **Young, W.C., Budynas, R.G. and Roark, R.J.** *"Roark's formulas for stress and strain".* 7th Edition. Boston : McGraw-Hill, 2002.

36. **Cleland, A.N.** *Foundations of Nanomechanics.* Berlin : Springer, 2003.

37. **S., Dohn.** "Cantilever Based Mass Sensing Alternative Readout and Operation Schemes". *Ph.D. Thesis.* s.l., Denmark : MIC - DTU, 2006.

38. **Mahmoodi, S.N., Afshari, M., and Jalili, N.** "Nonlinear Vibrations of Piezoelectric Microcantilevers for Biological Induced Surface Stress Sensing". *Journal of Communications in Nonlinear Science and Numerical Simulation.* 2008. Vol. 13, 9 pp. 1964-1977.

39. **Afshari, M.** "Nonlinear Modeling of the Adsorption-Induced Surface Stress in Piezoelectrically-Driven Microcantilever Biosensors". *Master Thesis.* s.l., South Carolina, USA : Clemson University, 2007.

40. **Zhang, Y. Ren, Q. and Zhao, Y.** "Modelling analysis of surface stress on a rectangular cantilever beam". *Journal of Physics D: Applied Physics.* 2004. Vol. 37, pp. 2140–2145.

41. **Stemme, G.** "Resonant silicon structures". *Sensors and Actuators.* 1989. Vol. 17, pp. 145-154.

42. **Davis, Z.** Masters Thesis. s.l., Denmark : MIC-DTU, 1999.

43. Atomic force microscope. *Wikipedia.* [Online] 2008. [Cited: March 10, 2008.] http://en.wikipedia.org/wiki/Atomic_force_microscope.

44. **Wiora, G., Schorsch.** Wikicommons. *Image:Laserprofilometer EN.* [Online] 2006. [Cited: March 13, 2008.] http://commons.wikimedia.org/wiki/Image:Laserprofilometer_EN.svg.

45. **Cray, B.A., Forsythe, S.E., Hull, A.J. and L. E. Estes.** "A scanning laser Doppler vibrometer acoustic array". *Journal of Accoustic Society of America.* 2006. Vol. 120, 1, pp. 164-170.

46. Photolithography. [Online] Georgia Tech. [Cited: March 15, 2008.] http://www.ece.gatech.edu/research/labs/vc/theory/photolith.html.

47. **Kujawa, P. and Winnik, F. M.** "Volumetric Studies of Aqueous Polymer Solutions Using Pressure Perturbation Calorimetry: A New Look at the Temperature-Induced Phase Transition of Poly(N-isopropylacrylamide) in Water and D2O". *Macromolecules.* 2001. Vol. 34, pp. 4130-4135.

48. **Sun, T., Wang, G., Feng, L., Liu, B., Ma, Y.,Jiang, L. and Zhu D.** "Reversible Switching between Superhydrophilicity and Superhydrophobicity". *Angewandte Chem.* 2004. Vol. 43, pp. 357-360.

49. **Cheng, X., Canavan, H. E., Stein, M. J., Hull, J. R., Kweskin S. J., Wagner, M. S., Somorjai, G. A., Castner, D. G., and Ratner B. D.** "Surface Chemical and Mechanical Properties of Plasma-Polymerized N-Isopropylacrylamide". *Langmuir.* 2005. Vol. 21, pp. 7833-7841.

50. **Beines, P. W., Klosterkamp, I., Menges, B., Jonas, U. and Knoll, W.** "Responsive Thin Hydrogel Layers from Photo-Cross-Linkable Poly(N-isopropylacrylamide) Terpolymers.". *Langmuir.* 2006. Vol. 23, pp. 2231-2238.

51. **Bradley, C., Nett, S., Chu, L., Berger, R., Jalili, N.** "Application of Static Mode Microcantilever Sensor for Precise Detection of Polymers Lower Critical Solution Temperature". *International Workshop on Nanomechanical Cantilever Sensors*. Mainz, Germany. 2008.

52. **Toda, M.** multi-cantilever-half. [Online] [Cited: March 22, 2008.] http://vip.nano.ee.es.osaka-u.ac.jp/~toda/images/multi-cantilever-half.jpg.

53. **Rasmussen, P.A., Hansen, O., Boisen A.** "Cantilever surface stress sensors with single-crystalline silicon piezoresistors". *Applied Physics Letters.* 2005. Vol. 86, 20.

54. **Johansson, A., Calleja, M., Rasmussen, P.A., Boisen, A.** "SU-8 cantilever sensor system with integrated readout". *Sensors Actuators A.* 2005. Vols. 123-124, pp. 111-115.

55. **Mo Li, Tang, H. X. and M. L. Roukes.** "Ultra-sensitive NEMS-based cantilevers for sensing, scanned probe and very high-frequency applications". *Nature Nanotechnology.* 2007. Vol. 2, 2.

56. **Frens, G.** 105, 1973, Physical Science Nature, Vol. 241, pp. 20-22.

57. **Zhang, W. and Turner, K.L.** A Mass Sensor Based on Parametric Resonance. 2004.

58. **Spletzer, M., Raman, A., Reifenberger, R., Wu, A. Q. and Xu, X.** "Ultrasensitive Mass Sensing Using Mode Localization in Coupled Microcantilevers". *International Workshop on Nanomechanical Sensors.* 2006.

59. **Zhang, W., Baskaran, R. and Turner, K. L.** "Tuning the Dynamic Behavior of Parametric Resonance in Micromechanical Oscillator". *Applied Physics Letters.* 2003. Vol. 82, p. 130.

60. **Epureanu, B. and Hashmi, A.** "Parameter Reconstruction Based on Sensitivity Vector Fields". *Journal of Vibration and Acoustics.* 2006. Vol. 82, p. 732.

61. **Jalili, N. and Olgac, N.** "Identification and Re-tuning of Optimum Delayed Feedback Vibration Absorber". *AIAA Journal of Guidance, Control, and Dynamics.* 2000. Vol. 23, p. 961.

62. **Jalili, N. and Olgac, N.** "Multiple Identical Delayed-Resonator Vibration Absorbers for Multi-Degree-of-Freedom Mechanical Structures". *Journal of Sound and Vibration, and Control.* 1999. Vol. 223, 4 pp. 567-585.

63. **Jalili, N. and Esmailzadeh, E.** "Optimum Active Vehicle Suspensions with Actuator Time Delay". *ASME Journal of Dynamic Systems, Measurements and Control.* 2001. Vol. 123, p. 54.

64. **Nayfeh, A. H.** *Nonlinear Interactions.* New Jersey : Wiley, 2000.

65. **Olgac, N. and Jalili, N.** "Modal analysis of flexible beams with delayed resonator vibration absorber: theory and experiments". *Journal of Sound and Vibration.* 1998. Vol. 218, 2, p. 567.

66. **Masoud, Z., Daqaq, M. and Nayfeh, N.** "Pendulation Reduction of Small Telescopic Cranes". *Journal of Vibration and Control.* 2004. Vol. 10, p. 1167.

67. **Daqaq, M. F., Bradley, C., Jalili, N., and Alhazza, K.** "Feedback Delays for Ultrasensative Sensing". *Proceedings of the ASME 2007 International Design Engineering Technical Conferences.* Las Vegas : s.n., 2007.

68. **Nayfeh, A. H., and Mook, D. T.** *Nonlinear Oscillations.* New York : Wiley-Interscience, 1979.

69. **Das, S. L. and Chatterjee, Y.** 'Multiple Scales without Center Manifold Reductions for Delayed Differential Equations near Hopf Bifurcations". *Nonlinear Dynamics.* 2003. Vol. 30, p. 323.

70. **He, J, -H.** "Periodic Solutions and Bifurcations of Delay Differential Equations". *Physics Letters A.* 2005. Vol. 347, p. 228.

71. **Bradley, C.R., Daqaq, M.F. and Jalili N.** "Experimental Study on Utilizing Delayed-Feedback for Ultra-Sensitive Sensing". *Proceedings of IMECE2007.* Seattle : s.n., 2007.

72. **Mahmoodi, S.N., Jalili, N., and Daqaq, M.F.** Modeling, Nonlinear Dynamics and Identification of a Piezoelectrically-Actuated Microcantilever Sensor. *IEEE/ASME Transactions on Mechatronics.* 2008. pp. 58-65.

73. **Jalili, N. and Esmailzadeh, E.** "A sensitivity study on optimum delayed feedback vibration absorber ". *Transactions of the ASME Journal of Dynamic Systems, Measurement and Control.* 2000. Vol. 122, 2, pp. 314-21.

74. **Roukes, M. L.** "Very-high-frequency nanocantilevers: Advances, physics, & applications". *International workshop on Nanomechanical Sensors.* 2006.